



**POLITECNICO**  
**MILANO 1863**

SCUOLA DI INGEGNERIA INDUSTRIALE  
E DELL'INFORMAZIONE

# Streamwise traveling waves of wall deformation for turbulent drag reduction

TESI DI LAUREA MAGISTRALE IN  
AERONAUTICAL ENGINEERING - INGEGNERIA AERONAUTICA

Author: **Nil Couto Ovejero**

Student ID: 966735

Advisor: Prof. Maurizio Quadrio

Academic Year: 2023-24



# Abstract

This study is aimed to investigate the net power saving rate in a turbulent channel flow when applying streamwise traveling waves of wall deformation. An in-house DNS code exploiting the Immersed Boundary method (IBM) is used to simulate the flow. The DNS code that originally used a hard coded parallelisation scheme has been updated with a new scheme based on the MPI library, and its scaling efficiency has been tested.

The plane channel is first validated with bibliographic references, and a parametric study is then performed by changing the wall velocity amplitude, wavelength and wave propagation speed of the downstream traveling peristaltic waves of wall deformation. The results confirm that the active flow control methodology applied is capable of reducing the pumping power required to drive the flow, translating into turbulent drag reduction. Two different behaviours are observed for the controlled cases: Some cases achieve full re-laminarization and remain in this flow regime for the rest of the simulations, while other cases are turbulent for the complete execution time even if they present net power savings.

**Keywords:** Computational Fluid Dynamics, Direct Numerical Simulation, Turbulence, Flow control, Peristalsis, Drag reduction, Immersed Boundary Methods



## Sommario

Questo studio si propone di analizzare il tasso di risparmio energetico netto in un flusso di canale turbolento quando si applicano onde di deformazione delle pareti che viaggiano lungo la corrente. Per la simulazione del flusso è stato utilizzato un codice DNS interno che sfrutta il metodo Immersed Boundary (IBM). Il codice DNS, che originariamente utilizzava uno schema di parallelizzazione hard coded, è stato aggiornato con un nuovo schema basato sulla libreria MPI ed è stata testata la sua efficienza di scala.

Il canale piano viene dapprima convalidato con riferimenti bibliografici, quindi viene eseguito uno studio parametrico modificando l'ampiezza della velocità della parete, la lunghezza d'onda e la velocità di propagazione delle onde peristaltiche di deformazione della parete a valle. I risultati confermano che la metodologia di controllo attivo del flusso applicata è in grado di ridurre la potenza di pompaggio necessaria per guidare il flusso, traducendosi in una riduzione della resistenza turbolenta. Per i casi controllati si osservano due comportamenti diversi: alcuni casi raggiungono la completa rilaminazione e rimangono in questo regime di flusso per il resto delle simulazioni, mentre altri casi rimangono turbolenti per tutto il tempo di esecuzione anche se presentano un risparmio netto di potenza.

**Parole chiave:** fluidodinamica computazionale, DNS, turbolenza, controllo del flusso, peristalsi, riduzione della resistenza aerodinamica, metodi ondari immersi



# Contents

<b>Abstract</b>	<b>i</b>
<b>Sommario</b>	<b>iii</b>
<b>Contents</b>	<b>v</b>
<b>List of Figures</b>	<b>vii</b>
<b>1 Introduction</b>	<b>1</b>
<b>2 Theoretical Background</b>	<b>3</b>
2.1 Turbulence fundamentals . . . . .	3
2.2 Governing equations . . . . .	5
2.3 Flow control strategies . . . . .	6
<b>3 Numerical implementation</b>	<b>11</b>
3.1 Governing Equations . . . . .	11
3.2 Time advancement . . . . .	11
3.3 Immersed boundary technique . . . . .	12
3.4 Code structure . . . . .	15
3.5 Parallelisation . . . . .	16
<b>4 Results</b>	<b>20</b>
4.1 Setup of the experiment . . . . .	20
4.2 Reference Case . . . . .	23
4.3 Peristalsis cases . . . . .	24
4.4 Re-laminarization Cases . . . . .	28
4.5 Turbulent Cases . . . . .	30
4.6 Net power saving rate . . . . .	34

5	Conclusions and future developments	38
	Bibliography	40
	Acknowledgements	44



# List of Figures

2.1	Flow visualization of a turbulent round jet. Data from Dimotakis <i>et.al</i> ,1983	4
2.2	Streamwise traveling waves of blowing and suction . . . . .	8
2.3	Traveling wave-like deforming walls . . . . .	9
3.1	Solid boundaries immersed in the Cartesian grid. [37] . . . . .	13
3.2	Parallel scheme . . . . .	17
3.3	Speed up . . . . .	17
3.4	Scaling efficiency . . . . .	18
4.1	Reference channel geometry with moving walls [27]. Axis modified to be consistent with the present configuration . . . . .	21
4.2	Normalized roots mean square fluctuation velocity components . . . . .	24
4.3	Roots mean squared fluctuation velocity components . . . . .	24
4.4	Mean streamwise pressure gradients. Reference — ; Laminar ---- ; case1 — ; case2 — ; case3 — ; case4 — ; case5 — ; case6 — ; case7 — ; case8 — ; case9 — ; case10 — ; case11 — . . . . .	26
4.5	Mean streamwise pressure gradients from [27] . . . . .	27
4.6	Turbulent kinetic energy for relaminarization cases . . . . .	28
4.7	Velocity field of <i>case01</i> in the y-z plane . . . . .	29
4.8	Velocity field of <i>case01</i> in the x-z plane . . . . .	29
4.9	Mean velocity profiles for <i>case01</i> at multiple streamwise positions and time instants . . . . .	30
4.10	Time history of <i>tke</i> . . . . .	31
4.11	Mean velocity profiles for <i>case04</i> . . . . .	31
4.12	Instantaneous root mean square fluctuation velocity components for <i>case04</i> (left) and <i>case05</i> (right) at three different streamwise locations . . . . .	33
4.13	Reynolds shear stresses for <i>case04</i> (left) and <i>case05</i> (right). $x = 1.5$ — ; $x = 3$ — ; $x = 4.5$ — . . . . .	34
4.14	Net power saving rate map as function of peristalsis inputs . . . . .	36

# 1 | Introduction

The aeronautical industry is facing one of the major challenges in aviation history: the reduction of  $CO_2$  emissions and a transition into a greener industry model. Given the high ecological impact of this industry, the development of more sustainable technologies is a fundamental step in the aviation history, ensuring an ethical model for the decades to come. Skin friction drag is a major component of the overall drag of airplanes, cars or other transport vehicles, reason why flow control strategies for drag reduction have been extensively researched for decades. Note that flow control techniques do not only affect drag reduction, and consequently fuel consumption, but also stability, maneuverability, aircraft endurance or noise reduction.

Flow control strategies can be divided in two categories: Passive and Active. Passive flow control techniques are based on geometry modifications that doesn't introduce external energy to the system (e.g riblets), while active techniques introduces energy into the system (e.g moving walls). Both approaches have demonstrated to be able to reduce drag under different conditions and drag components (friction drag and pressure drag), even though active flow control shows better drag reduction at the expense of adding complexity in the procedures.

The present Thesis focuses on the study of active flow control strategies, among with traveling waves of blowing and suction and travelling waves of wall deformation are probably the most popular approaches. Both strategies are closely related as shown in Hoepffner and Fukagata in 2009 [15], and following this line of research Nakanishi, Mamori and Fukagata in 2012 [27] studied the relaminarization of a turbulent channel flow using traveling wave-like wall deformation. They proved that streamwise traveling waves of wall deformation are capable of drastically reduce drag (especially in those cases that were relaminarized), and that this reduction can be translated into net power savings. In more recent studies, Fukagata, Iwamoto and Hasegawa in 2024 [11] suggest that the beneficial effects of streamwise traveling waves of wall deformation persist for practically high Reynolds numbers ( $Re_\tau \sim 10^5$ ), even though a further experimental validation should be performed according to the authors.

The objective of this Thesis is to implement peristaltic moving walls (streamwise traveling waves of wall deformation) with an in-house DNS code in order to replicate the results obtained by Nakanishi et. al in 2012 [27], and to analyze up to which extent net power savings can be achieved. The in-house DNS code used was first developed by Secchi in 2018 [37], who adapted an already existing Immersed Boundary method flow solver (produced by Paolo Luchini) in order to account also for non-planar moving walls. Nevertheless, this code used a hard-coded parallelisation scheme, which has been updated in the present Thesis with a parallelisation scheme exploiting the MPI library. DNS applications is a crucial part of the project. This computational approach to solve the discretized governing equations is the most powerful approach among RANS and LES in terms of accuracy, given that DNS is a model-free approach for the near-wall region. However, DNS simulations need large computational power to be executed, requiring of High Performance Computing (HPC) resources as well as highly efficient codes. For this reason the in-house code used exploits an Immersed Boundary method for the wall treatment, allowing to use a non body conformal Cartesian grid constant in time that reduces memory consumption and computational costs.

The present Thesis is structured as follows: The theoretical background presented in Chapter 2 introduces the main characteristics of turbulent flows and a brief explanation of the main flow control strategies with special focus on peristaltic moving walls. In Chapter 3 the numerical aspects of the solution procedure are presented, with a special focus on the IB method exploited and reporting the scaling efficiency test results. At the beginning of Chapter 4, the set-up of the experiments is presented. With the problem and numerical strategy described at this point, the results divided into relaminarization and ordinary reduction cases are later presented in Chapter 4, with a final section dedicated to the net power savings. Finally, in Chapter 5, the main results are discussed together with suggestions for future developments.

# 2 | Theoretical Background

## 2.1. Turbulence fundamentals

Turbulent flows remain as one of the most prevalent and challenging phenomena encountered in real-world engineering applications. Unlike laminar flows, which present an ordered and predictable behavior, turbulent flows are characterized by the dominance of inertial forces, leading to an unsteady, chaotic and unpredictable behaviour. Fig.2.1 is intended to exemplify the complexity of turbulent flows, and the extent diversity of shapes that vortical structures can present. Despite its extensive presence in nature, turbulence remains one of the most significant unsolved problems in physics. Nevertheless, through extensive research during multiple decades, the primary mechanisms governing turbulent motions have been established.

Particularly in near-wall regions, turbulence sustains itself through a cyclical and spatially organized process [13]. During this process high-speed fluid is driven towards the wall, while low-speed fluid is ejected from it, resulting in a distinctive flow pattern known as 'streaks'. This pattern is characterized by alternating bands of slow- and fast-moving fluid observed within the inner layers of shear flows [18]. Runstadler in 1967 [20] made the hypothesis that the production of turbulence was largely due to busting of the 'streak' patterns in the inner layers of the boundary layer, and precisely to the release of low-speed streaks. The hypothesis also included that the bursting events are also dominant in the energy transfer in the entire turbulent shear layer [20]. This last hypothesis leads to the fact that turbulent flows improve the mixing of heat, mass and momentum with respect to laminar flows. The enhanced mixing of momentum for turbulent flows produces larger wall shear stress with respect to laminar flows, while enhanced rates of heat and mass transfer at solid-fluid and liquid-gas interfaces are also achieved by turbulent flows [32]. In order to discriminate from laminar and turbulent flows, it's crucial to introduce the Reynolds number  $Re = \frac{UL}{\nu}$ , where  $U$  is the reference velocity,  $L$  the reference length and  $\nu$  is the kinematic viscosity of the fluid. Reynolds number is a dimensionless quantity that represents the ratio between inertial and viscous forces. Therefore, for a low Reynolds number the flow stays laminar while an increase on  $Re$  above a critical value would en-

tail a turbulent motion and instabilities in the flow. As summarized in [30], the major motivation behind the study of turbulent flows is the combination of the vast extent of turbulent flows in nature, the transport and mixing of matter, momentum, and heat in flows has huge practical importance, and that turbulence greatly enhances the rates of the mentioned processes.



Figure 2.1: Flow visualization of a turbulent round jet. Data from Dimotakis *et.al*,1983

Coherent structures in turbulent flows can be defined as regions of concentrated vorticity, characteristic and flow-specific organization, recurrence, appreciable lifetime and scale [33], even though multiple definitions have been formulated by many authors (see Robinson 1991, Hussain 1987 ). A more in-detail description of the coherent structures is presented in this paragraph following [35]. As it has been previously mention, the near-wall turbulence-production arises from the streaks confined in the buffer layer. In the flow's outer region, three-dimensional bulks of the scale of the boundary-layer thickness are generated. These structures are responsible of pulling free-stream non-turbulent fluid into the turbulent region and the generation of large, weakly rotational eddies beneath the bulges. The interaction between high-speed fluid and the upstream sides of the large scales produce shear layers of the scale of the viscous length. There's therefore a dynamical relationship between the inner region, where production cycle is largely self-sustained, and the outer structure that is believed to have a modulating influence in the processes confined at the vicinity of the wall. The problem of this dynamic relationship remains open still today. Kline, Robinson & Spalart in 1989 [34] proposed the following classification of the multiple coherent structures reported in literature:

1. Low-speed streaks in the viscous sublayer

2. Ejections of low-speed fluid outward from the wall
3. Sweeps of high-speed fluid inward toward the wall
4. Vortical structures of various forms (e.g Horseshoe and hairpin vortical structures)
5. Sloping near-wall shear layers
6. Near-wall regions clean of near-wall fluid
7. Large motions driven by the three-dimensional bulges
8. Large-scale outer region motions

## 2.2. Governing equations

For the problem considered, the governing equations are the continuity equation and the viscous, unsteady, incompressible momentum equation, which are defined in the following form:

$$\nabla \cdot \mathbf{u} = 0 \quad (2.1)$$

$$\frac{\partial \mathbf{u}}{\partial t} + (\mathbf{u} \cdot \nabla) \mathbf{u} = -\nabla p + \nu \nabla^2 \mathbf{u} \quad (2.2)$$

where  $\mathbf{u}$  is the velocity vector,  $p$  is the pressure  $P$  divided by the fluid density  $\rho$  and  $\nu$  is the kinematic viscosity of the fluid. The components  $x$ ,  $y$  and  $z$  defining the channel directions, and their associated velocity component  $u$ ,  $v$ ,  $w$ , correspond to the streamwise, spanwise and wall-normal (with respect to the reference plane channel). Applying the well known Reynolds decomposition, we can separate a flow variable (e.g the velocity  $\mathbf{u}$ ) into the mean and fluctuating components, as shown in Eq.(2.3).

$$u(x, y, z, t) = \bar{u}(z) + u'(x, y, z, t) \quad (2.3)$$

Given that a plane channel flow has 2 homogeneous directions ( $x$  streamwise and  $y$  spanwise), we can compute the mean component of a flow variable by space and time averaging it by applying the following definitions :

$$u_{xy}(z, t) = \frac{1}{L_x L_y} \int_0^{L_x} \int_0^{L_y} u(x, y, z, t) dx dy \quad (2.4)$$

$$\bar{u}(z) = \lim_{T \rightarrow \infty} \frac{1}{T} \int_0^T u_{xy}(z, t) dt \quad (2.5)$$

### 2.3. Flow control strategies

Flow control technologies, whereas they act actively or passively, have the objective to modify the flow behaviour around a given surface. The objective of these modifications is to improve the aerodynamic efficiency, control the transition from laminar to turbulent, prevent/induce flow separation, enhance/eliminate turbulence, suppress flow-induced noise, etc. [1]. Given the motivations of the present Thesis, both passive and active techniques presented in this section will be focused on the drag reduction capabilities. A brief literature review for both passive and active techniques is presented below, together with an in detail description of peristaltic waves of moving walls.

The friction drag coefficient  $C_f$  of a fully-developed turbulent channel flow is computed by using a weighted integration of the Reynolds shear stress  $(-\overline{u'w'})$  [8][4] :

$$C_f = \frac{12}{Re_b} + 24 \int_0^1 (1-z)(-\overline{u'w'})dz \quad (2.6)$$

Observing Eq.2.6 it's clear than in case of a laminar flow, the only contribution to  $C_f$  would be the first element in the summation given that no velocity fluctuations  $u'$  and  $w'$  are present for a laminar flow. Therefore, we call the first term the laminar contribution. The second contribution is a weighted average of Reynolds shear stress. Note that the weighting  $(1-z)$ , being  $z$  the distance from the wall, attributes a larger weight to the near-wall region since it's where the main mechanisms responsible of friction drag production are confined. The aim of flow control technologies (passive and active) is to reduce the second term in Eq.2.6, or equivalently the Reynolds shear stress. Following this logic, if the second term becomes negative enough, a sub-laminar level could be achieved according to the previous identity [25]. A more detailed description of this possibility is presented later when presenting the traveling wave-like blowing and suction approach.

#### Passive flow control

As it's been anticipated in Chapter1, passive flow control techniques are characterized by the absence of energy injection into the fluid, leading to simpler implementations with respect to active techniques. Among passive flow control strategies, riblets are one of the most extensively studied devices to reduce drag in near-wall regions [42], showing drag reduction rates between 7%- 8% [41]. The efficiency of riblets increase if the groove is aligned with the streamwise direction of the flow, further reducing turbulent drag [6]. For this type of devices, a key parameter is the protrusion height, defined as the distance

between the tip of the riblet and the mean origin of the velocity profile, resulting in what can be interpreted as a slip length. An increase in drag reduction caused by an increase in streamwise velocity is observed in case that the streamwise slip acts at the plane of riblet tips [12].

Another approach for passive techniques is to modify the flow behaviour without introducing any component, but instead control it with the roughness of the material itself. An example of this approach are superhydrophobic surfaces, characterized by the presence of micro or nano cavities that trap fluid particles dropping the skin friction in the fluid-solid boundary [36]. However, this technique has only been tested in experimental setups given that the trapped fluid particles cannot hold under real operation conditions. More common surface related passive strategies are turbulators or high roughness bands, even though this techniques are mainly used for a controlled boundary layer separation instead of drag reduction [17]

The last passive flow control strategy presented is compliant surfaces, which are thin deformable surfaces driven by the flow in contact with, and without any external energy input. Compliant surfaces can be isotropic or anisotropic plates suspended by springs connected to a rigid wall that contract/expand depending on the force produced by the fluid flow [5]. When in contact with flows of turbulent nature, anisotropic compliant surfaces tend to deform by streamwise traveling waves, which is able to produce negative distributions of Reynolds shear stress at the surface vicinity [9]. However, relatively low drag reduction rates can be achieved with this strategy, and its application is still very limited except for research purposes.

## Active flow control: Streamwise traveling waves of blowing and suction and streamwise traveling waves of wall deformation

Even though many Passive Flow Control technologies such as riblets have been successfully applied showing drag reduction rates, the aeronautical industry has had a growing interest on Active Flow Control (AFC) during the last decades, as it allows to be activated under certain situations and in different parts of the airplane independently. Even if the list of AFC technologies is large, including synthetic jets, valves and plasma actuators, this section will focus on two approaches only, given the importance they have for the problem at hand. This two techniques are streamwise traveling waves of blowing and suction and streamwise traveling waves of wall deformation.



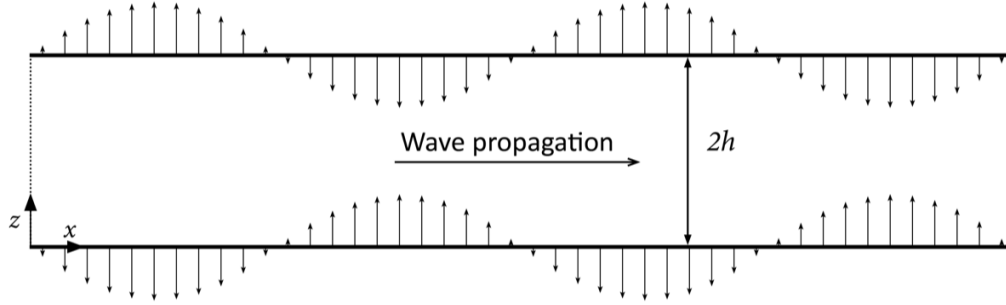


Figure 2.2: Streamwise traveling waves of blowing and suction

Bewley in 2001 [2] stated that the minimum drag achievable in a turbulent channel flow controlled through traveling waves of blowing and suction is exactly that of the ideal laminar flow. Based on Eq.2.6, Min et al. in 2006 [25], and applying a control model based on traveling wave-like blowing and suction from the walls, demonstrated that in case of upstream traveling waves it's possible to largely decrease the Reynolds shear stresses, and as a consequence skin-friction drag. In addition, and under a specific set of parameters, it was also demonstrated that it's possible to reduce drag to a sub-laminar level by making the second term in Eq.2.6 negative enough to counter the laminar drag, which was not supported in Bewley's conjecture. The fact that a sub-laminar drag can be achieved does not entail that the total power needed to pump the flow is also lower than the pumping power of the laminar case, but instead the power required is always larger than for the reference laminar case [10] [3]. Given this condition, it can be stated that the ultimate goal for drag reduction in a channel flow is to achieve relaminarization.

A substantial difference between the two active flow control techniques described was reported by Hoepfgner and Fukagata in 2009 [15], who found that traveling walls or peristalsis (explained in detail in the following paragraph) requires a pumping in the same direction than the traveling waves, while in the wave-like blowing and suction method the pumping is in the opposite direction. For the latest case, drag reduction under a constant flow rate is a combination of the direction of the pumping effect and stability. In fact, both Moarref and Jovanović in 2010 [26] and Lee et.al in 2008 [21] stated that upstream traveling wave-like blowing and suction derives into an unstable behaviour and promote turbulence, while downstream traveling waves are stable and capable of sustaining a laminar flow.

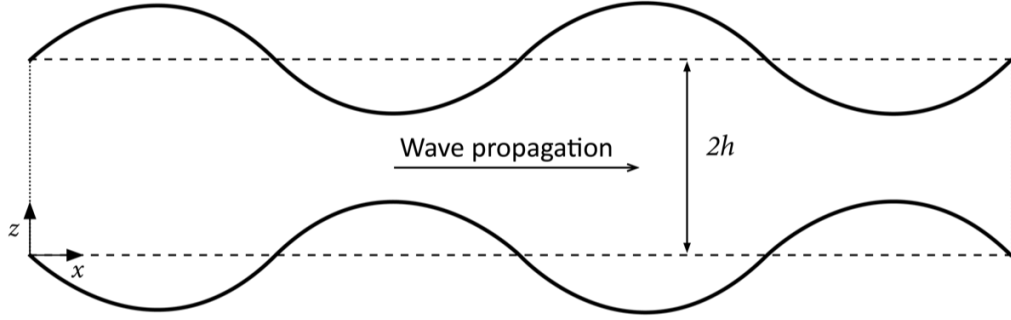


Figure 2.3: Traveling wave-like deforming walls

The second active flow control methodology presented is traveling wave-like deforming walls, which is the methodology selected in the present Thesis to achieve drag reduction. This technique arose from the findings obtained when studying wave-like blowing and suction, and it's less costly to test in real experiments since a lower the number of peristalsis actuators is needed with respect to blowing/suction actuators, as well as an easier physical implementation. The previous paragraph stated that drag reduction using peristalsis is caused by downstream traveling waves, given that the pumping direction is reversed with respect to the alternative method. In addition, this technique present larger stability [21] [27], enhancing the relaminarized flows to stay in this condition.

Taneda and Tomonari in 1973 [40] already highlighted the potential of this technique, and they observed experimentaly that dountstream traveling waves at a wavespeed higher than the uniform flow lead to laminarization under a certain set of parameters. In addition, they observed that a cyclically transition from laminar to turbulent and viceversa can also be obtained under the proper peristalsis input parameters. Similar research was performed by Shen et. al in 2003 [38], but in this case using DNS. They observed how local relaminarization appears when the wavespeed is larger than the freestream velocity of the flow, and that the resulting net power and total drag is reduced with respect to the case where sttionary waves are employed. A substantial difference between Taneda and Tomonari (1973) and the implementation for this project is that, in the present Thesis, the amplitude of wall deformation is in the order of the thickness of viscous layer, while the previous publication considered amplitudes of the order of the boundary layer thickness. Among the extent research done regarding this topic, Nakanishi et. al (2012) is of great importance for the present Thesis, since the aim of the project is to replicate the results presented in this publication. Nakanishi et. al studied the effects peristalsis deformation in a fully developed turbulent channel flow by means of DNS. It demonstrated that not

only friction drag is reduced under the conditions mentioned above, but also that the flow can be completely relaminarized (no turbulence surviving) under certain configurations of the velocity amplitude, wave-number and phase-speed of wall deformation.

# 3 | Numerical implementation

## 3.1. Governing Equations

The flow considered in the present work is viscous, unsteady and incompressible. Therefore, the flow is govern by the Navier-Stokes equations in non-dimensional form, which read:

$$\frac{\partial u_i}{\partial x_i} = 0 \quad (3.1)$$

$$\frac{\partial u_i}{\partial t} + \frac{\partial u_i u_j}{\partial x_j} + \frac{\partial p}{\partial x_i} - \frac{1}{Re} \frac{\partial^2 u_i}{\partial x_j \partial x_j} = F_i \quad i = 1, 2, 3 \quad (3.2)$$

Where  $u_i$  are the velocity components,  $x_i$  are the Cartesian coordinates,  $p$  is the pressure,  $Re$  is the Reynolds number and  $F_i$  is the forcing term. From this point on, quantities in dimensional form are denoted with an asterisk. The Reynolds number is defined as:

$$Re = \frac{U^* h^*}{\nu^*} \quad (3.3)$$

Where  $U^*$  is the reference velocity,  $h^*$  the reference length scale and  $\nu^*$  is the fluid kinematic viscosity. Given that the reference geometry is a plane channel represented by two walls distancing  $2\delta^*$ , all dimensional variables are nondimensionalized by using the mean bulk velocity  $U_b^*$  and the half channel height  $\delta^*$ . As a consequence, the reference bulk Reynolds number is defined as  $Re_b = \frac{U_b^* \delta^*}{\nu^*}$

## 3.2. Time advancement

Time advancement is performed using a fully explicit third-order Runge Kutta method, meaning that a given time-step is divided into three sub-steps and a fractional step technique is applied at each sub-step independently. The fractional step approach applied to perform the numerical integration of the governing equations is based on a multi-step

avancement of Eq.3.2. The momentum equation Eq.3.2 is first advanced in time without accounting for the continuity equation Eq.3.1, and the compressibility constraint is enforced afterwards during the projection step, when the velocity field is projected into the solenoidal vector-field and the pressure field is updated accordingly at the same time. The procedure described can be written in the following way:

Knowing the velocity  $u_{ix,iy,iz}^k$  at a given grid point at the sub-step  $k$ , the intermediate velocity  $\hat{u}_{ix,iy,iz}^{k+1}$  at the sub-step  $(k+1)$  is computed such that:

$$\hat{u}_{ix,iy,iz}^{k+1} = u_{ix,iy,iz}^k + \alpha_k \Delta t LNL(u_{ix,iy,iz}^k) + \beta_k \Delta t LNL(u_{ix,y,iz}^{k-1}) + (\alpha_k + \beta_k) \Delta t [F^k - G(p^k)] \quad (3.4)$$

Being  $\alpha_k$  and  $\beta_k$  the Runge Kutta method coefficients,  $LNL(\cdot)$  is the sum of the linear  $L(\cdot)$  and non linear  $NL(\cdot)$  discretized operators and  $G(\cdot)$  is the discretized gradient operator, all present in Eq.3.2. Following the steps of the Runge Kutta methods, the computed intermediate velocity field  $\hat{u}_{ix,iy,iz}^{k+1}$  has to be projected into the field of solenoidal vector field by:

$$u_{ix,y,iz}^{k+1} = \hat{u}_{ix,iy,iz}^{k+1} - G(\phi_{ix,iy,iz}^{k+1}) \quad (3.5)$$

Where  $\phi$  is the pseudo-pressure computed with the Poisson equation Eq.3.6. Note that in practice a Black-Red SOR algorithm is applied to solve the linear system arising from the Poisson equation:

$$\nabla^2 \phi^{k+1} = \nabla \cdot \hat{u}^{k+1} \quad (3.6)$$

Once  $\phi_{ix,iy,iz}^{k+1}$  is computed, the pressure field at the sub-step  $k+1$  can be updated with:

$$p_{ix,iy,iz}^{k+1} = p^k + \frac{\phi_{ix,iy,iz}^{k+1}}{(\alpha_k + \beta_k) \Delta t} \quad (3.7)$$

### 3.3. Immersed boundary technique

The position and velocity of a point of the wall are given by Eq.3.8 and Eq.3.9.

$$\begin{cases} z = z_l(x, y, t) & \text{lower wall} \\ z = z_u(x, y, t) & \text{upper wall} \end{cases} \quad (3.8)$$

$$\begin{cases} U_l = w_l(x, y, t) \hat{z} & \text{lower wall} \\ U_u = w_u(x, y, t) \hat{z} & \text{upper wall} \end{cases} \quad (3.9)$$

Where  $z_l$  and  $z_u$  are the expressions for the wall position,  $w_l$  and  $w_u$  its time-derivative respectively and  $\hat{z}$  the unit vector in wall-normal direction. Following this declaration, and applying no-slip boundary conditions, the velocity of the fluid at any point of the solid walls with respect to the reference axes must be as reported in Eq. 3.10.

$$\begin{aligned} u(x, y, z, t) = v(x, y, z, t) = 0; w(x, y, z, t) = w_l(x, y, z, t) \quad \text{at} \quad z = z_l(x, y, t) \\ u(x, y, z, t) = v(x, y, z, t) = 0; w(x, y, z, t) = w_u(x, y, z, t) \quad \text{at} \quad z = z_u(x, y, t) \end{aligned} \quad (3.10)$$

As it has been already mentioned, the code exploits the usage of an Immersed Boundary method. This method was first conceived by Peskin in 1972 [28] for the treatment of fluid-structure (fiber) interactions around heart valves. Based on this publication, multiple research studies have followed this approach to study the solid-fluid interaction with rigid [39] [24] and elastic bodies [29]. One of the implications of this method is that the boundary conditions in Eq. 3.10 can rarely be imposed straight forward because of the the grid doesn't adapt to the solid boundaries but instead it remains constant in time. Therefore, the boundary between solid walls and fluid is usually placed inside of a grid element (see Fig.3.1), which requires the treatment described in this section to impose the boundary conditions.

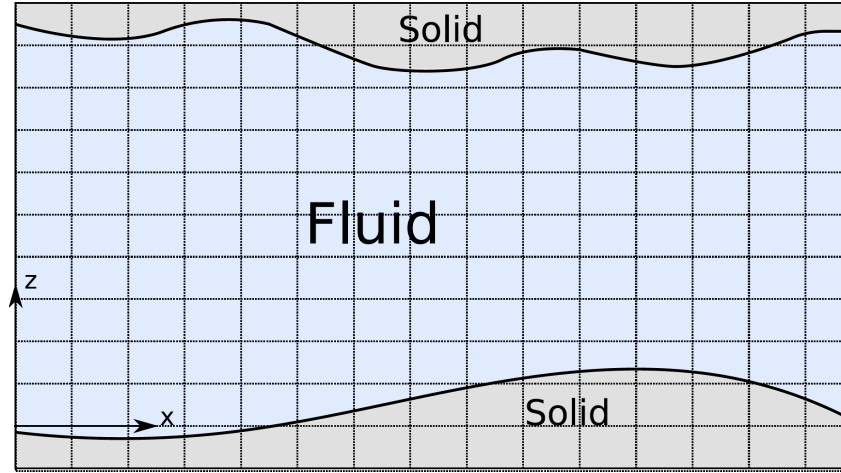


Figure 3.1: Solid boundaries immersed in the Cartesian grid. [37]

For the sake of simplicity the steps are presented for a 2-D channel with non-null velocity in the wall-normal direction of the solid boundaries (for a more detailed description see [37]). Then this same step is repeated for the different planes completing the three-dimensional domain. A second simplification has been considered for the following explanation, using

the explicit Euler method instead of the Runge-Kutta method. The later has been already covered in the previous section, but involves a level of complexity not necessary to show the steps needed for BC imposition. The velocity component in z-direction at time-step  $n+1$  is:

$$\tilde{w}_{ix,iz}^{n+1} = w_{ix,iz}^n + \Delta t [L(w_{ix,iz}^n) + NL(w_{ix,iz}^n, w_{ix,iz}^{n+1}) - G_z(p_{ix,iz}^n)] \quad (3.11)$$

Note that  $(\tilde{\cdot})$  denotes that the velocity component does not account for the wall boundary condition yet. Regarding the terms between square brackets, the operators  $L(\cdot)$ ,  $NL(\cdot)$  and  $G_z(\cdot)$  are evaluated using the velocity and pressure respectively at given point at the previous time-step  $n$ . Therefore also these terms are computed without accounting for the boundary position at time-step  $n + 1$ . This inconsistency is solved by applying a correction  $C$  to Eq. 3.11, more precisely coming from the linear term  $L(\cdot)$ . The correction on  $L(\cdot)$  is motivated by the fact that this term is responsible of the main contribution in momentum's balance in regions close to the solid boundaries. Thus, the computation of  $L(\cdot)$  accounting for the location of the boundary is:

$$L(w_{ix,iz}) = \frac{1}{Re_b} \left[ \frac{w_{ix-1,iz} + w_{ix+1,iz}}{\Delta x^2} + \frac{W_{IB}}{\delta \Delta z} + \frac{w_{ix,iz+1}}{\Delta z^2} - \left( \frac{2}{\Delta x^2} + \frac{1}{\Delta z^2} + \frac{1}{\delta \Delta z} \right) w_{ix,iz} \right] \quad (3.12)$$

This correction is introduced to Eq.(3.10) by means of the mentioned correction  $C$ . Recalling the momentum equation Eq.(3.2), the linear term  $L(\cdot)$  would be:

$$L(w_{ix,iz}) = \frac{1}{Re_b} \left[ \frac{w_{ix-1,iz} + w_{ix+1,iz}}{\Delta x^2} + \frac{w_{ix,iz+1} + W_{IB}}{\Delta z^2} - \left( \frac{2}{\Delta x^2} + \frac{2}{\Delta z^2} \right) w_{ix,iz} \right] \quad (3.13)$$

Then, the correction term  $C$  is obtained by comparing Eq.(3.13) and Eq.(3.12), and included in the momentum equation Eq.(3.4) through the vertical velocity:

$$C = c_1 w_{ix,iz} - c_2 W_{IB} \quad (3.14)$$

$$\tilde{w}_{ix,iz}^{n+1} = w_{ix,iz}^{n+1} + \Delta t C \quad (3.15)$$

Finally, Eq.3.14 can be computed by directly using the velocity at the time-step  $n+1$  in Eq.3.15, allowing to directly compute  $w_{ix,iz}^{n+1}$ :

$$w_{ix,iz}^{n+1} = \frac{\tilde{w}_{ix,iz}^{n+1}}{1 + c_1 \Delta t} + \frac{c_2 \Delta t}{1 + c_1 \Delta t} W_{IB} \quad (3.16)$$

### 3.4. Code structure

The code is written in CPL, a general purpose programming language based on C and Fortran and developed by Paolo Luchini [22]. In order to implement the numerical schemes previously presented, the code is divided in the following files:

- `channel.cpl`
- `iofiles.cpl`
- `parallelbcs.cpl`
- `parallelbcs.h`
- `timestep.cpl`

The main script is **channel.cpl**. It first reads all the geometric, fluid properties and peristalsis input data required from a *.dat* file or an initial field. Based on the peristaltic input data, the analytic expression of the shape and BCs of the bottom and top walls can be defined independently. A boolean function for each wall called *bwall* and *twall* are later used during the time-marching to track which grid-points lie inside of the solid walls. Then the time-loop starts and the solution is advanced in time. The sub-routines performed at each timestep are: **calcimbc**, **timestep**, **savefield** and **output**. The sub-routine **calcimbc** computes the IB method coefficients for the corresponding wall position at that given time instant. The functions *bwall* and *twall* are then used to compute the IB coefficients for all solid boundaries. At each position in the x-y plane, a pointer variable to a 1-D array of size  $[0..nz]$  stores the IB coefficients that identify those nodes whose numerical stencil crosses the wall boundary. At the start of the timeloop the subroutine **calcimbc** is called three times, one per each velocity components, and the IB coefficients arrays are updated at each time-step. The **timestep** subroutine declared in **timestep.cpl** is called three consecutive times to perform the multiple Runge-Kutta method sub-steps for time-marching. The sub-routine **savefield** saves the current flow-field in *.field* format after a selected number of iterations, while **output** is used to monitor certain run-time quantities like the external time units or the mean pressure gradient. It also allows to save the time history of selected quantities in a *.dat* file.

**iofiles.cpl** contains the sub-routine declarations needed for reading or writing data. Firstly we can choose whether to initialize the simulation with an analytic expression for the velocity profile or by reading an already existing flow-field in *.field* format. Both options have been used during different stages of the project. The previously mentioned **savefield** and **output** are included in `iofiles.cpl`.



**parallelbcs.cpl** and **parallelbcs.h** are responsible for the parallel computation by two or more processors. Here a crucial part of the project was carried out, as the code now exploits the MPI library features to perform parallel computing. The number of processors and its distribution across the domain (number of processors in x and y direction) is declared in **parallelbcs.h**. It also includes the subroutine responsible for MPI initialization and internal communication. **parallelbcs.cpl** include subroutines related to parallel execution and periodic boundary conditions. As a result, this file is also necessary for enforcing periodic boundary conditions for serial executions.

The subroutine **timestep** responsible of performing the Runge-Kutta method for time-marching is declared inside of **timestep.cpl** together with the subroutines **linestep** and **pressurelinestep**, both called inside of **timestep** subroutine through a loop for all grid-locations in the horizontal plane. The **linestep** subroutine performs the time advancement of the momentum equation for each velocity component at all the grid nodes in the z-direction at a given point in the horizontal plane. The **pressurelinestep** subroutine projects the intermediate velocity field into the space of solenoidal vectors while updates the pressure field. This is performed using a red-black successive over-relaxation (SOR) algorithm that results in lower memory usage. If CFR is used like in the present case, the velocity field and mean pressure gradient are updated according to the difference between imposed flowrate and the computed flowrate.

### 3.5. Parallelisation

It is possible to separate the computational domain into different sections across the streamwise and spanwise directions and dedicate a machine to each partition, resulting in faster simulations. Fig. 3.2 shows a segment of the channel in the X-Y plane divided in four parts, and each partition has been assigned a different machine. The arrows on the right side of the figure (after the partition of the domain) show how the transfer of information between machines only occurs at the boundaries of adjacent partitions. The flow-field is updated at each time-step through two steps: The inner nodes of the partition are updated in first place, and once all the adjacent machines have finished this task the boundary region is updated, resulting in an almost partition-independent advancement of the governing equations.

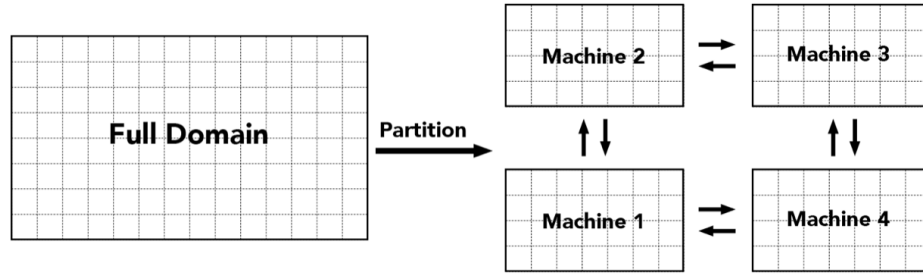


Figure 3.2: Parallel scheme

A proper implementation of parallel computation strategies is a key factor when dealing with HPC resources. For this reason an analysis based on the speed-up  $S$  and scaling efficiency  $E$  has been performed in order to select the optimal configuration in terms of parallel performance. Note that the scaling study has been performed with the mesh used for the peristalsis validation, composed of  $n_x=400$ ,  $n_y=112$ ,  $n_z=260$ , using the Galileo100 supercomputer at CINECA computing center. The speed-up is the ratio of the execution time for the serial task to the time for the parallel task, which read:

$$S = \frac{\Delta t_S}{\Delta t_P} \quad (3.17)$$

Where  $\Delta t_S$  is the time needed to perform a given number of iterations (in this case 10 iterations) in serial and  $\Delta t_P$  the time required using  $P$  machines. Fig. 3.3 presents the computed speed-up using 2, 4, 8, 16, 32 and 48 machines, and it is observed how the efficiency scales positively up to 32 machines, showing a decrease of speed up for  $P=48$ .

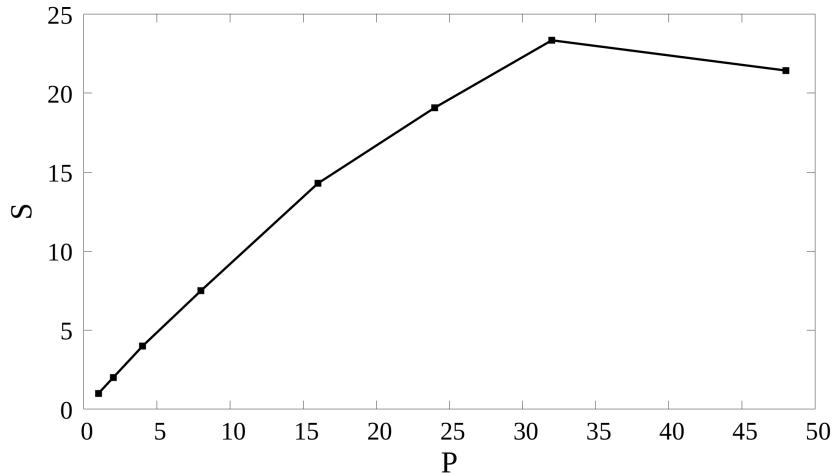


Figure 3.3: Speed up

The efficiency of the scaling  $E$  is computed as:

$$E = \frac{S}{P} \quad (3.18)$$

Where  $P$  is the number of machines used and  $S$  the previously computed speed-up. The ideal value of efficiency is 1, which could only be achieved if the ideal linear scaling holds, which does not in reality. The efficiency computed for the same set of machines as for the speed up is presented in Fig. 3.4.

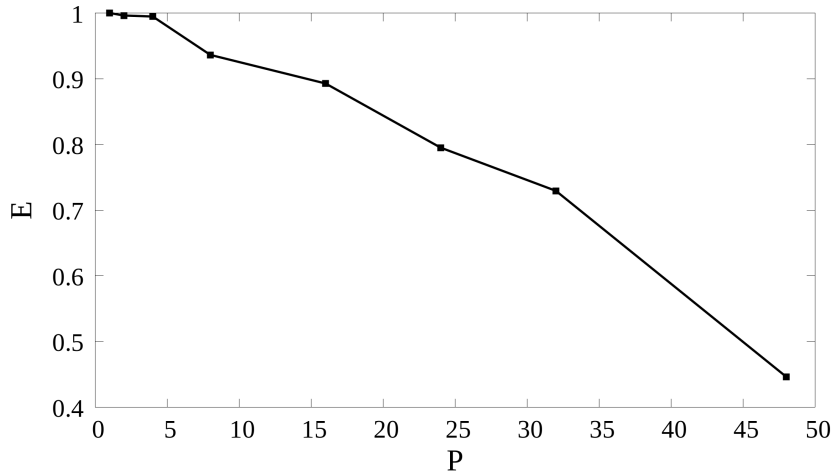


Figure 3.4: Scaling efficiency

Similarly to Fig.3.3, the scaling efficiency decreases faster from  $P=32$ . By observing both  $S$  and  $P$  it can be concluded that the most efficient number of processors is 32. However, Galileo100's computing nodes are composed of 48 cores, reason why it was first decided to scale the number of processors down to  $P=24$ , resulting in a better efficiency and the possibility of running two cases simultaneously with a single node.

One of the main milestones of the present Thesis was to update the parallelisation strategy used in the code, switching from a hard-coded parallelisation scheme to exploiting MPI. Open MPI is an open source Message Passing Interface library used for parallel computation and developed by a consortium of academic, research and industry partners. Note that the OpenMPI implementation was included in the *parallels.h* file explained in Sec.3.4. When experimenting with the code, it was noticed that spurious oscillations appear when  $nx \neq ny$ , while the solution is spurious-free if the condition  $nx = ny$  is respected. This issue is possibly arising from a bug in the MPI implementation that should be further investigated in future applications of the code. Given the limited time available to perform a considerable amount of simulations, together with the fact that even if the

speed-up is not optimal for  $P=16$  it shows an efficiency  $E = 0.9$ , it was decided to proceed with the preliminary parallel scheme with  $P=16$ . Note that by using 16 processors, two simultaneous simulations can be executed with a single node. Therefore, the reference case has been validated and the peristalsis cases simulated, under this configuration.

One drawback of Immersed Boundary methods is that spurious oscillations may appear as a consequence of the movement of solid boundaries with respect to the nodes of the Cartesian grid [23]. Since walls have a prescribed movement but the grid is static, grid elements close to the solid boundaries get covered and cleared by the solid boundaries at each timestep. This situation produces the non conservation of total fluid volume, which can be enforced by choosing the time-step considering the movement of the wall in such a way that for a given time-step solid boundaries cover the same number of nodes. The relationship applied to fulfill this condition must therefore be related to the phase speed of the wall deformation  $c$ :

$$\frac{c\Delta t}{\Delta x} = 1 \quad (3.19)$$

## 4 | Results

In order to validate the Immersed Boundary method previously presented, and to test the application of peristalsis actuators for drag reduction, a parametric study based on the characterizing parameters of the wall actuation  $a$ ,  $c$  and  $k$  has been performed using DNS simulations. The different cases studied with their corresponding wall actuation parameters are presented in Tab. 4.3. Note that since the grid is constant for all the parametric study, and following Eq. 3.19 presented when discussing the spurious oscillations resulting from a violation of volume conservation, the time-step  $\Delta t$  only changes according to the phase-speed  $c$ . The maximum wall height is defined as  $\frac{a}{kc}$ , and given that  $L_z = 2.2$  for the computational domain, the maximum wall height cannot exceed  $\frac{a}{kc} = 0.1$  so they can be allocated properly into the computational domain.

### 4.1. Setup of the experiment

The geometry considered in the present project is a channel flow composed of two movable solid walls where no-slip boundary conditions have to be applied. A particularity of the numerical implementation is that the code is based on an Immersed Boundary algorithm in order to enforce the boundary conditions. This strategy entails a static grid that doesn't adapt to the wall position, but instead the solid surfaces are taken into account by correcting the governing equations in those elements which computational stencil intersect the channel boundaries.

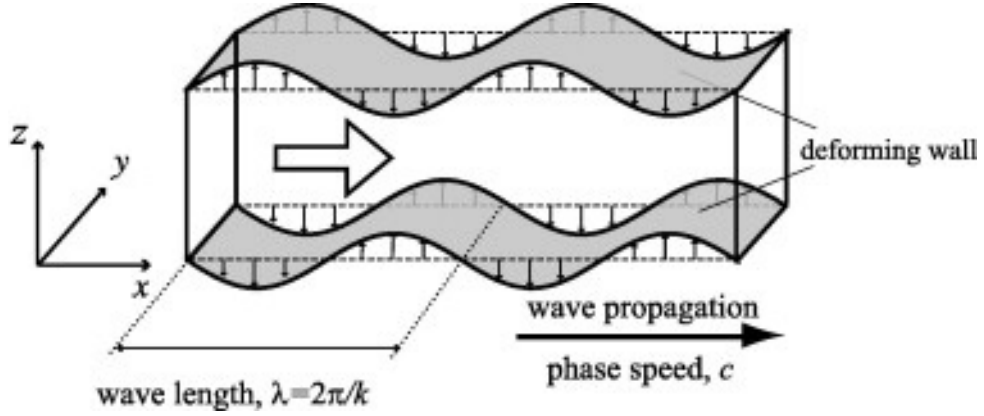


Figure 4.1: Reference channel geometry with moving walls [27]. Axis modified to be consistent with the present configuration

The position of the movable walls is defined with the analytic form for the top and bottom solid walls independently, in this case both sinusoidal functions. A similar implementation is followed for the wall velocity boundary condition. Note that the walls are only allowed in the  $z$ -direction, therefore in the wall-normal direction:

$$\begin{cases} z_b = -\frac{a}{kc} \sin[k(x - ct)] & \text{Lower wall} \\ z_t = 2 + \frac{a}{kc} \sin[k(x - ct)] & \text{Upper wall} \end{cases} \quad (4.1)$$

$$\begin{cases} u = v = 0, & w_b = a \cos[k(x - ct)] & \text{for } z = z_b \\ u = v = 0, & w_t = -a \cos[k(x - ct)] & \text{for } z = z_t \end{cases} \quad (4.2)$$

Where  $a$  is the wall velocity amplitude,  $k$  the wavelength and  $c$  is the wave propagation speed of the downstream traveling peristaltic waves. These three parameters will be the input parameters used during the peristalsis tests.

A computational domain with  $L_x = 2\pi$  and  $L_y = \pi$  in the streamwise and spanwise directions respectively was first used to work with the code on the local machine, while a larger computational domain of  $L_x = 4\pi$  and  $L_y = 3.5$  was later used for all the simulations performed exploiting HPC. For the wall normal direction, even if the plane channel height is  $2\delta^*$ , being  $\delta^*$  the dimensional channel half-height, the height of the computational domain has been set to  $L_z = 2.2$  in order to have enough space to allocate the walls when peristalsis is applied. The selection of the domain size and grid resolution was based on previous DNS studies with the same objective [37] [27].

Mesh	$L_x$	$L_y$	$L_z$	<b>nx</b>	<b>ny</b>	<b>nz</b>
Testing	$2\pi$	$\pi$	2.2	80	80	100
Validation	$4\pi$	3.5	2.2	400	112	260

Table 4.1: Meshes used

For the rest of the report, quantities with an asterisk will refer to dimensional quantities. The two quantities used for all physical quantities dimensionless are the half channel-height  $\delta^*$  and the mean bulk velocity  $U_b^*$ . Using the definitions for the computation of mean components presented early in this chapter, we can define the dimensionless bulk velocity  $U_b$  as:

$$U_b = \frac{1}{2h} \int_0^{2h} \bar{u}(z) dz \quad (4.3)$$

The Reynolds number  $Re_b$  is described as:

$$Re_b = \frac{U_b^* \delta^*}{\nu^*} \quad (4.4)$$

Where  $\nu^*$  is the kinematic viscosity of the fluid. Since both  $U_b^*$  and  $\delta^*$  correspond the unit for the present case (separation between walls for the plane channel is 2),  $Re_b$  could be also expressed as  $Re_b = \frac{1}{\nu^*}$ . In order to match the conditions in [27], the Reynolds number has been set to  $Re_b = 2800$ , entailing  $\nu^* = 3.57e - 4$ , and the corresponding friction Reynolds number is  $Re_\tau = \frac{u_\tau^* \delta^*}{\nu^*} \approx 180$  for the plane channel.

Following [31], three possible approaches can be considered when dealing with turbulent flows through channels: constant pressure gradient (CPG), constant flow-rate (CFR) and constant power input (CPI)[14]. In CPG simulations, the flow is under a constant pressure gradient and the flow-rate can vary, while CFR enforces a prescribed flow-rate, and the mean pressure gradient is responsible of adjusting the flow to respect the prescribed condition. CPI is a combination of the 2 previous approaches, since the prescribed value is the product of flow-rate and mean pressure gradient, and both quantities are free to change independently to respect this condition. CFR has been selected as the approach used for all the simulations performed. This approach selection also dictates that the reference velocity has to be  $U_b^*$  [31], and therefore all velocities are made non-dimensional using  $U_b^*$ . Contrarily, if a CPG approach had been selected, the proper reference velocity should be  $u_\tau$ .

## 4.2. Reference Case

It's important to set a reference to which compare the results once wall-normal wall motion is introduced. For this reason, the results corresponding to the uncontrolled plane channel flow must be presented in great detail given the importance it will have when extracting conclusions. Similarly to the other simulations included in the present project, the reference case has been simulated for 1000 external time units, with sampling performed every 10 external time units. The validation of the results have been performed by comparing the resulting statistics with those presented by Kim, Moin and Moser [19] (KMM). Observing Tab.4.2 it can be seen how the computed mean flow properties are in great agreement with the reference data, and the small differences in the results may be a consequence of the differences in the mesh resolution and the usage of a spectral method by KMM. The mean flow properties have been computed by applying the space average and time average in Eq.2.4 and Eq.2.5 respectively, and the skin-friction coefficient  $C_f$  is non-dimensionalized using the mean bulk velocity  $U_b$ .

	Validation	KMM [19]
$Re_b$	2800	$\approx 2800$
$Re_\tau$	176.4	$\approx 180$
$Re_c$	3276	$\approx 3300$
$u_\tau$	0.063	0.064
$\delta_\nu$	0.0055	0.0056
$C_f$	$8.16 \cdot 10^{-3}$	$8.18 \cdot 10^{-3}$
$U_b/u_\tau$	15.87	15.63
$U_c/u_\tau$	18.57	18.20
$U_c/U_b$	1.17	1.16

Table 4.2: Reference case validation

The velocity fluctuation components are defined with respect to the corresponding component of the turbulent plane channel mean flow  $\bar{\mathbf{u}}(z)$  and computed applying Eq.2.3. The root-mean-square velocity fluctuation components  $u_{rms}$ ,  $v_{rms}$ ,  $w_{rms}$ , normalized by the reference skin-friction velocity  $u_{tau}$ , are presented in Fig.4.6. The shape of the profiles are in great accordance with the theory, with a peak of  $u_{rms} = 2.72$  at  $z^+ = 14.12$ ,  $v_{rms} = 1.09$  at  $z^+ = 35.66$  and  $w_{rms} = 0.84$  at  $z^+ = 55.66$ , expressed in wall units.



Reynolds shear stress  $-\overline{u'w'}$  is shown in Fig.4.3, and the shape of the profile is again in accordance with the expected solution. The symmetry of both the *rms* fluctuation velocities and the Reynolds shear stress with respect to the centerline of the channel suggest that the external time units were enough to ensure a converged solution as well as the sampling frequency was sufficient to compute statistics during the post-processing.

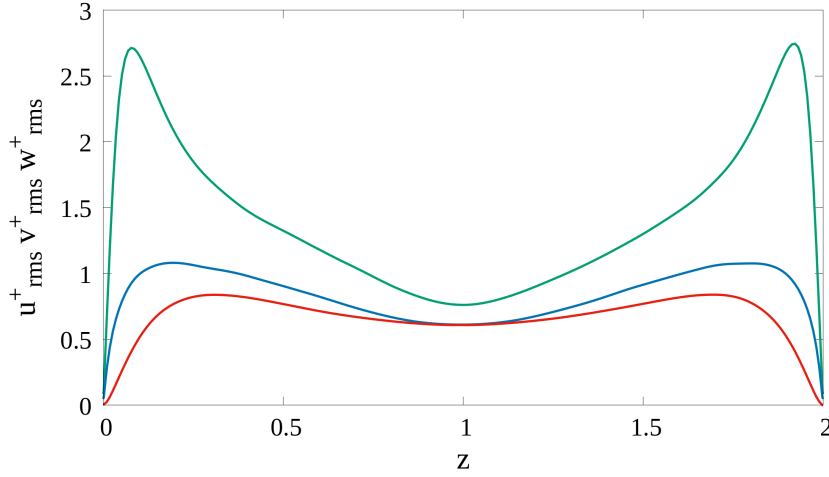


Figure 4.2: Normalized roots mean square fluctuation velocity components

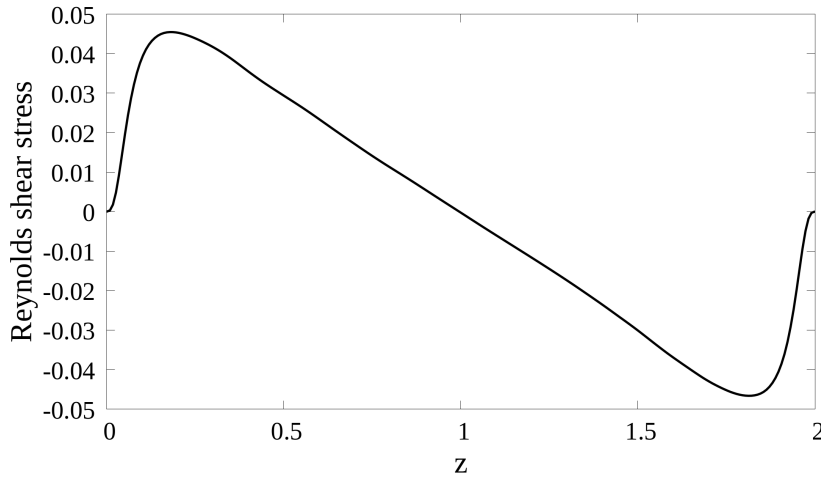


Figure 4.3: Roots mean squared fluctuation velocity components

### 4.3. Peristalsis cases

Once the reference case was established and validated in terms of mean flow properties and flow statistics, the set of controlled simulations presented in Tab.4.3 were executed and post-processed. Note that the peristalsis cases are expressed with respect to the wall

velocity amplitude  $a$ , the wavelength  $k$  and the wave propagation speed  $c$ , following the analytical expression of the wall and B.Cs in Eq.4.1 and Eq.4.2.

Case	<b>a</b>	<b>c</b>	<b>k</b>	Max. wall height	Equivalent case in [27]
Reference case	0	0	0	-	-
1	0.3	2	2	0.075	8
2	0.3	2	4	0.0375	9
3	0.4	2	2	0.1	11
4	0.2	2	1	0.1	4
5	0.1	2	1	0.05	1
6	0.2	2	4	0.025	6
7	0.1	6	4	0.004	14
8	0.1	2	2	0.025	2
9	0.2	6	2	0.017	15
10	0.2	6	4	0.008	16
11	0.4	2	4	0.05	12

Table 4.3: Peristalsis cases simulated

At this point it's important to divide the different peristalsis cases tested into two main groups based on its behaviour: Re-laminarized cases and turbulent cases. In Fig.4.4 the run-time solution of the mean pressure gradient for the controlled cases, the reference case and the theoretical laminar case are presented. The latter can be obtained from the exact solution of the Poiseuille plane channel:

$$-\frac{\overline{dP}}{dx} = \frac{3}{Re_b} = 1.0714 \cdot 10^{-3} \quad (4.5)$$

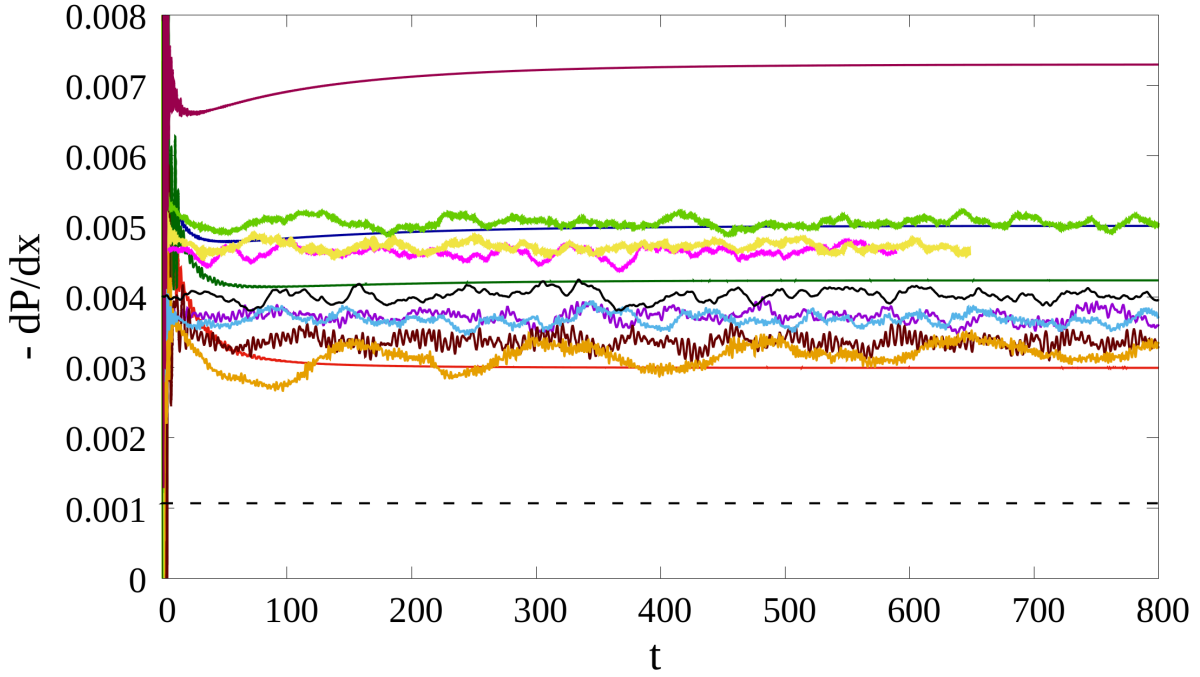


Figure 4.4: Mean streamwise pressure gradients. Reference — ; Laminar ---- ; case1 — ; case2 — ; case3 — ; case4 — ; case5 — ; case6 — ; case7 — ; case8 — ; case9 — ; case10 — ; case11 —

Observing Fig.4.4 it can be seen that, in the same fashion as the reference case, some controlled cases remain turbulent for the entire simulation time with a noisy mean streamwise pressure gradient. On the other hand, cases like *case01*, *case02* and *case03* clearly become laminar, converging to a given mean pressure gradient after approximately 100 external time units and remaining in this regime until the end of the simulations. It's important to highlight that the mean streamwise pressure gradient presented is the sum of two contributions: The external pressure gradient used to pump the flow and a peristaltic contribution induced by wall motion. Later in this section, a more detailed explanation regarding the treatment of the mean streamwise pressure gradient is presented with the objective of computing the net power saving.

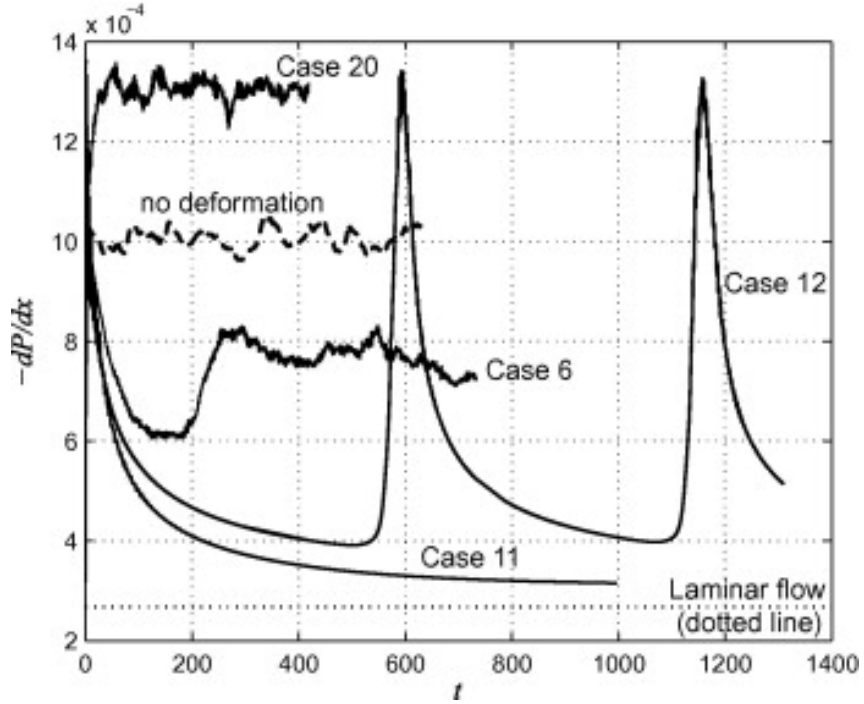


Figure 4.5: Mean streamwise pressure gradients from [27]

The results obtained in [27] are presented in Fig.4.5 for the sake of comparison, since the replication of this data is one of the goals of the present Thesis. The first observation to be done is the order of magnitude of the time traces, which are an order of magnitude lower than the data obtained with the in-house DNS code. The reasoning behind it is that Nakanishi et. al 2012 used a bulk velocity  $2U_b$ , resulting in  $Re_b = 5600$ . Therefore, a scaling of  $\frac{1}{4}$  can be applied to represent the results with the same reference values. Focusing on the equivalent cases for both figures, *case06*, *case11* and *case12* in Fig.4.5 are equivalent to cases *case06*, *case03* and *case11* in Fig.4.4, respectively. The first thing to notice is that even if applying the scaling previously mentioned, mean pressure gradient are not equivalent. The reason of this difference is that Nakanishi et. al (2012) presented only the mean pressure gradient needed to drive the flow, and therefore not accounting for the pumping power needed for wall actuation. Contrarily, the run-time mean pressure gradient computed by the in-house DNS code accounts for both contributions for the pressure gradient, resulting in larger numerical values. Nevertheless, a clear correlation for the equivalent cases can be observed: *case11* indicates a drastic drag reduction by achieving relaminarization, the same situation as for *case03* computed, while both *case06* remain turbulent for the whole extent of the simulations even if presenting ordinary drag reduction. *case12* from Nakanishi et. al (2012) shows the particularity that it becomes cyclically laminar, with sudden spikes in the mean pressure gradient that bring the flow to

a turbulent state. The in-house DNS code used is not able to capture the quick increase in turbulence, and in this case the flow remains laminar for the whole extent of the simulations. The reason why the code cannot capture this behaviour should be further investigated in future research.

#### 4.4. Re-laminarization Cases

In this section, *case1*, *case2* and *case3* are presented in detail to asses the cases than become laminar when peristalsis is applied. Turbulent kinetic energy *tke* is the mean kinetic energy per unit mass associated with eddies in turbulent flows. *tke* is defined as half the sum of the variances of the fluctuating velocity components, or analogously half the trace of Reynolds stress tensor:

$$tke = \frac{1}{2} \left( \overline{(u')^2} + \overline{(v')^2} + \overline{(w')^2} \right) \quad (4.6)$$

Where  $\overline{(u')^2}$ ,  $\overline{(v')^2}$  and  $\overline{(w')^2}$  are the variances of the streamwise, spanwise and wall-normal velocity fluctuations respectively. Fig.4.6 shows the time history of *tke* for cases 1,2,3 together with the reference turbulent channel flow. The lack of smoothness in the data, specially observable for the plane channel case, is due to the computation of *tke* during post-processing instead of run-time, and therefore reducing the sampling frequency of the solution. It can be clearly seen how the controlled cases tend to a laminar regime after approximately 200 external time units, and remain laminar until the end of the simulation. On the other hand, turbulence for the reference plane channel is sustained during time with  $\overline{tke} = 0.0069$ .

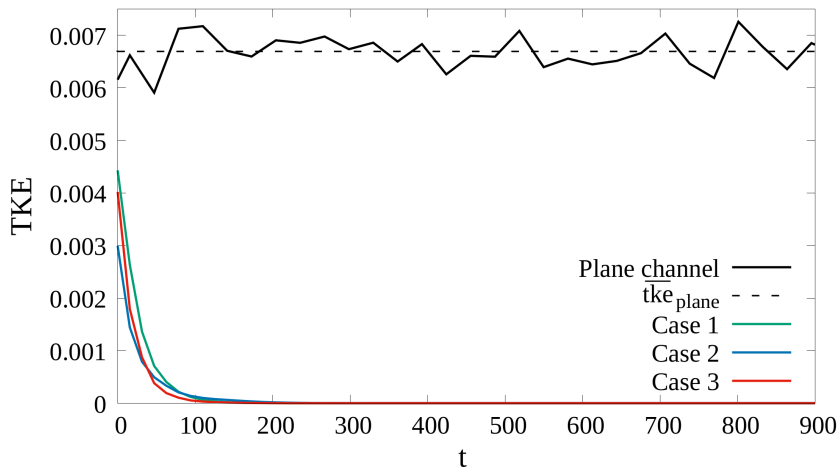


Figure 4.6: Turbulent kinetic energy for relaminarizarion cases

The velocity field of *case01* in Fig.4.7 and Fig.4.8 show the velocity field in spanwise and streamwise sections of *case01* at the initial and final external time units to better visualize the transition from turbulent to laminar. At  $t = 0 \frac{h}{U_b}$  the velocity field is clearly turbulent, with large vortical structures at the near-wall region, and the wall deformation with a sinusoidal function is also visible. At  $t = 1000 \frac{h}{U_b}$ , corresponding to the final flowfield generated, relaminarization is achieved showing an ordered flowfield with no presence of eddies at any region in the domain, and that remains layered at the vicinity of the walls.

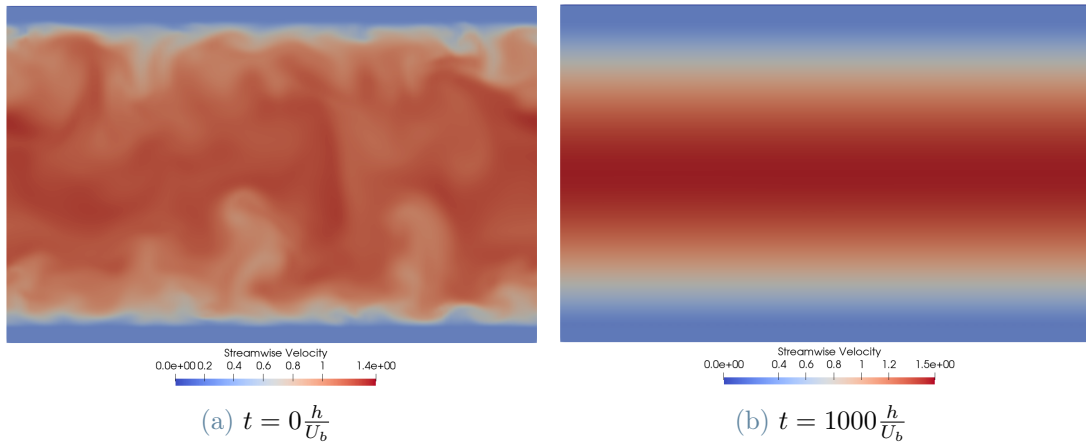


Figure 4.7: Velocity field of *case01* in the y-z plane

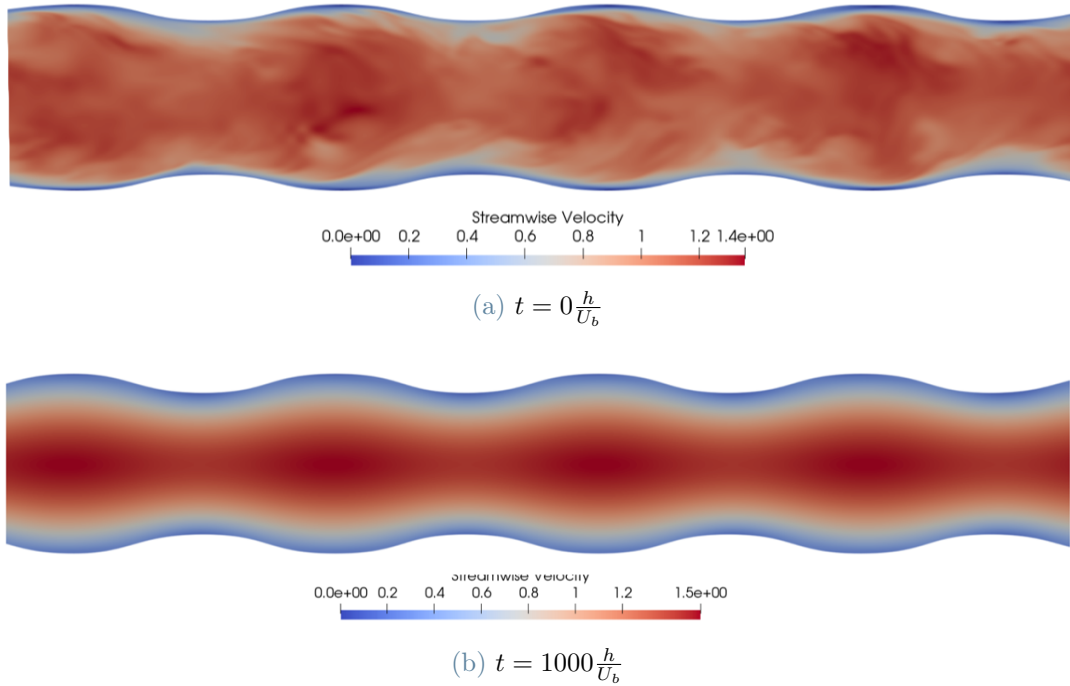


Figure 4.8: Velocity field of *case01* in the x-z plane

To further analyze the previous evolution, the mean velocity profiles at different streamwise positions for *case01*, the turbulent plane channel and the laminar plane channel at the initial and final time instants are presented in Fig.4.9. At  $t = 0 \frac{h}{U_b}$  the instantaneous mean velocity profile of *case01* presents a flattened shape characteristic of turbulent mean velocity profiles, and resembles the shape of the mean profiles for the reference plane channel case. Once relaminarization is achieved the velocity profile shows a parabolic-like shape that tend to the Poiseuille laminar profiles. Reverse flow can be observed for the controlled velocity profile at streamwise location  $x = 2.5$ , which according to [15] it is a consequence of the boundary movement that is responsible for transferring fluid particles in closed loop tracks.

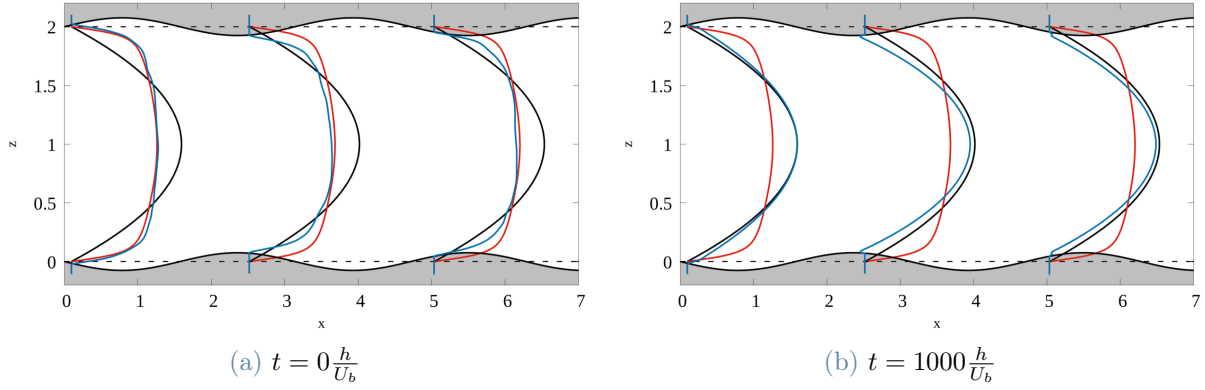


Figure 4.9: Mean velocity profiles for *case01* at multiple streamwise positions and time instants

## 4.5. Turbulent Cases

For the sake of simplicity, even if multiple studied cases remain turbulent for the full extent of the simulations, the time history of *tke*, mean velocity profiles and *r.m.s* of turbulent intensities are presented only for *case04* and *case05*. The rest of turbulent cases are accounted for at the net-power saving study in Sec.4.6. Both *case04* and *case05* remain turbulent until the end of the simulation as seen in Fig.4.10, but they present a lower *tke* with respect to the reference case for the complete time history. The mean *tke* for these cases is  $\overline{tke}_{04} = 0.00613$  and  $\overline{tke}_{05} = 0.0051$ , which indicates that even if they remain turbulent, ordinary drag reduction is achieved. The sustainment of turbulence is reflected in Fig.4.11, where for both time instants the velocity profile of *case04* has a flattened shape that resembles the turbulent profile of the plane channel. The irregularities in the controlled profile is because the profiles presented for the controlled cases are instantaneous, and therefore no time averaged or space averaged. The fact that the mean

velocity profile exceeds the reference profile at the second streamwise location, while falling behind for the third streamwise location, points to the fact that even if the mean flow-rate for the whole channel is enforced through the CFR approach, locally the flow-rate is not conserved.

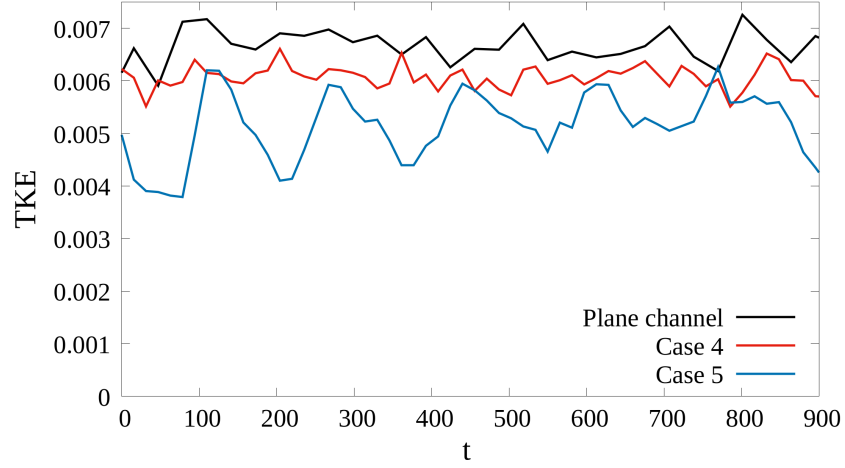


Figure 4.10: Time history of  $tke$

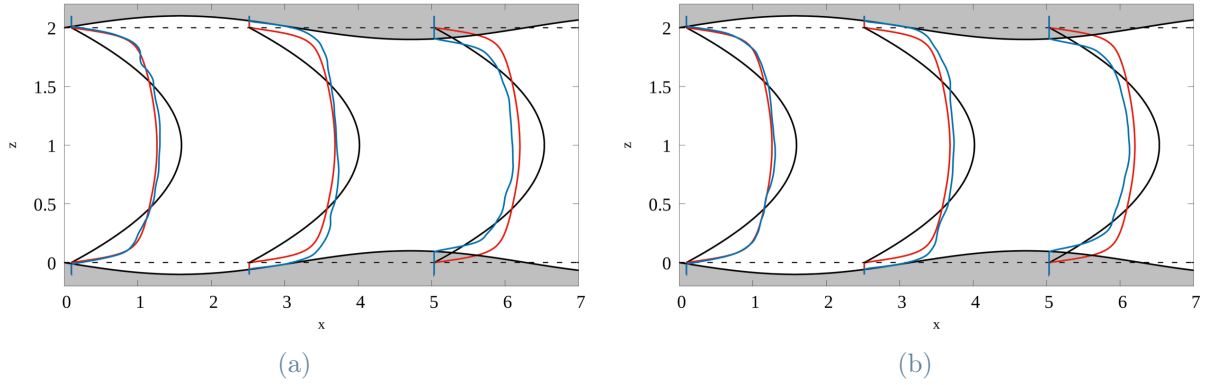


Figure 4.11: Mean velocity profiles for case04

Another significant statistic to compute is the root mean square fluctuation velocity components. In Fig. 4.12, *r.m.s* fluctuating velocity component normalized with bulk velocity are presented for multiple streamwise locations with the aim of investigating how the wall movement affect the Reynolds shear stress locally. The streamwise locations chosen represent characteristic points in the sinusoidal function describing the wall: The streamwise location  $x = 1.5$  corresponds to the most negative point of the bottom wall,  $x = 3$  refers to the point where the amplitude is null and  $x = 4.5$  is related to the point with maximum height in the bottom wall. From Fig.4.12, it can be confirmed that the introduction of



non-planar moving walls have an impact on the wall vicinity in terms of velocity fluctuations. At the streamwise location  $x=1.5$ , corresponding to the lowest point in the sinusoidal wave, the *r.m.s* profiles are shifted towards  $z$ -negative values, even displacing the fluctuation peaks into this region. Even if displaced, the intensity of the velocity fluctuations remain almost equal to the reference case, with a small reduction of its magnitude after the profile peaks. The difference in the amplitude of the sinusoidal functions in Fig. 4.12(a) and Fig. 4.12(b) is easily recognizable by the difference in the shift with respect to  $z=0$ . In the streamwise location  $x=2$ , corresponding to the point where no effective wall amplitude is present, the profiles resemble those corresponding to the plane channel, with only a small increase for the streamwise component's peak, and a slight reduction for the other two components. Finally, for the streamwise location  $x = 4.5$ , corresponding to the maximum height of the walls, the profiles for the controlled cases are again shifted but this time towards the center of the channel. A reduction of the turbulent intensity is visible, with lower peaks for both cases with respect to the plane channel. As it has been previously mentioned in Chapter 2, Reynolds shear stresses play a crucial role in drag reduction applications, and its reduction could lead to a re-laminarized flow and, eventually, sub-laminar drag. Given its importance in non-planar moving walls applications, Reynolds shear stresses for *case04* (left) and *case05* (right) for the same streamwise locations studied for the *r.m.s* analysis is presented in 4.13. The highly irregular shapes of the profiles is because the data presented (except for the reference case) is instantaneous. It's clear that  $-\overline{u'w'}$  is reduced with respect to the reference case, demonstrating again that peristalsis is capable to modify the behaviour of the flow at the wall-vicinity. Negative RSS can be observed for both cases at location  $x = 3$ , and at  $x = 1.5$  also for *case04*. This phenomenon is crucial for drag reduction because the more negative RSS are, the higher the reduction of skin-friction drag as anticipated earlier.

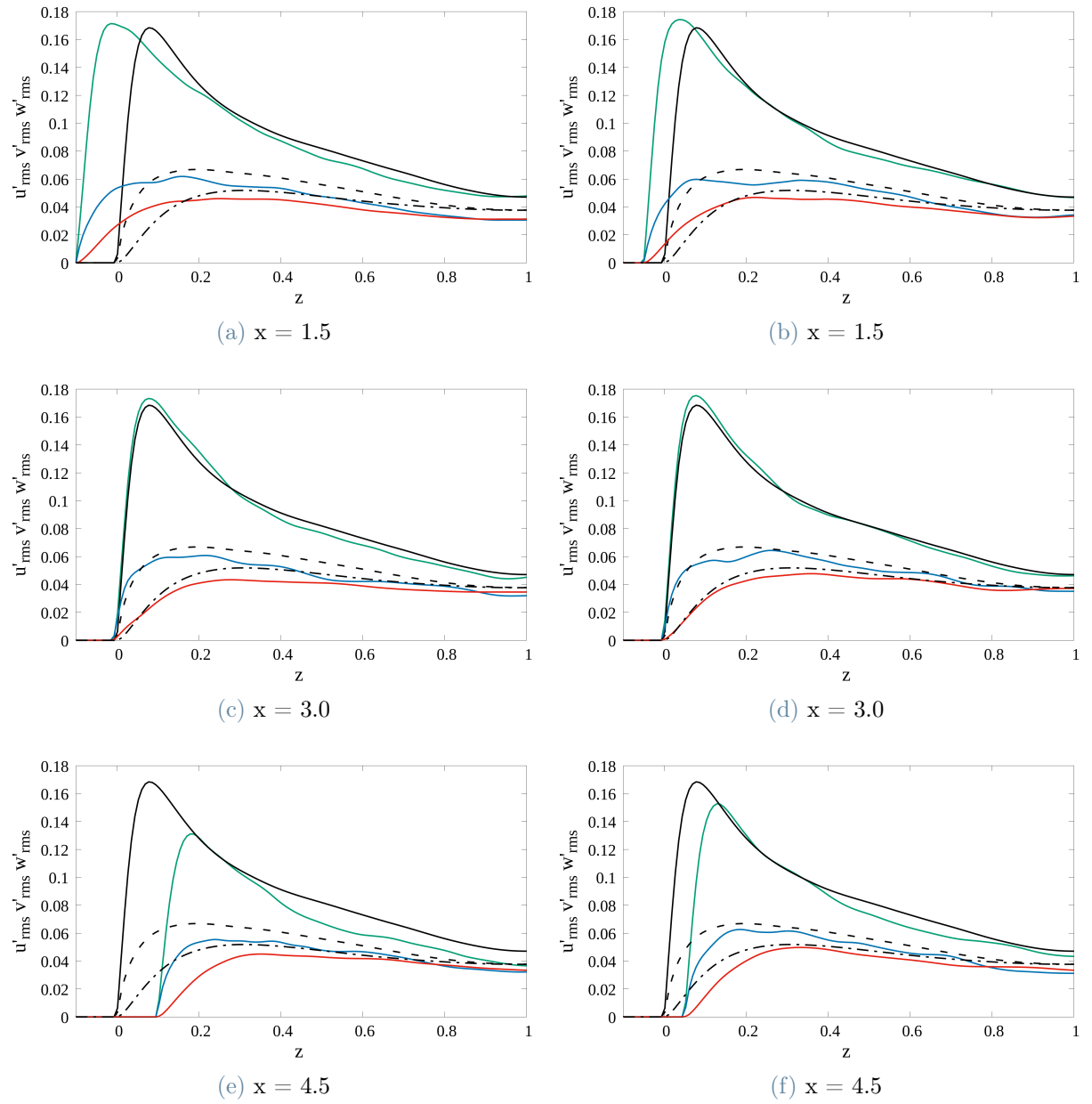


Figure 4.12: Instantaneous root mean square fluctuation velocity components for *case04* (left) and *case05* (right) at three different streamwise locations

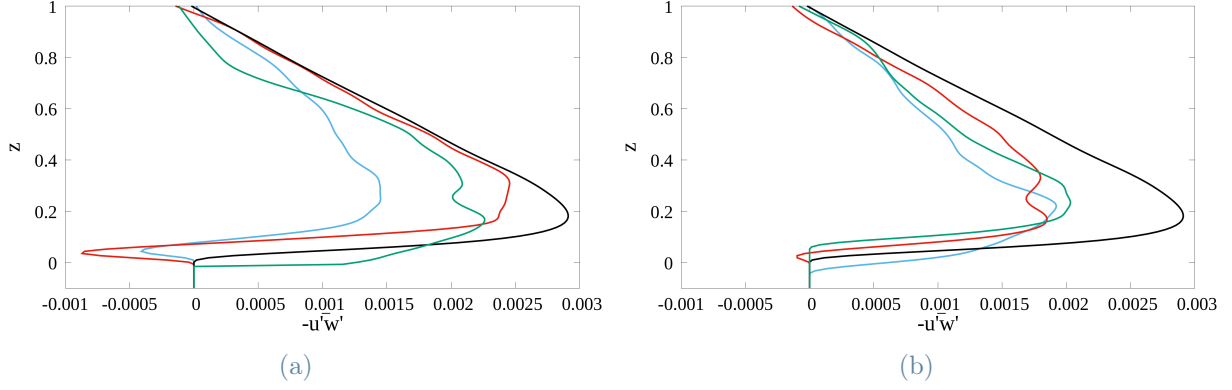


Figure 4.13: Reynolds shear stresses for *case04* (left) and *case05* (right).  $x = 1.5$  — ;  $x = 3$  — ;  $x = 4.5$  —

## 4.6. Net power saving rate

In Sec.4.2 it has been anticipated that the run-time streamwise mean pressure gradient is the sum of two contributions: the external pressure gradient and the peristaltic contribution. For this reason, the computation of the net power saving rate  $S$  is performed with the total dissipation  $\varepsilon$  instead of  $\frac{dP}{dx}$ . As explained in [10], at the statistically steady state the total dissipation  $\varepsilon$  can be described as:

$$\varepsilon = P_f + P_p + P_i \quad (4.7)$$

Where  $P_f$  is the friction power coefficient,  $P_p$  the pressure power coefficient and  $P_i$  the input power coefficient. Therefore, the sum of  $P_f$  and  $P_p$  correspond to the pumping power while  $P_i$  corresponds to the power required for peristalsis. Total dissipation  $\varepsilon$  can be described as:

$$\varepsilon = \frac{2}{Re_b V} \int_V \mathbf{S} : \mathbf{S} dV \quad (4.8)$$

Where  $S$  is the strain rate tensor,  $V$  the fluid volume and  $:$  is the double dot tensor product  $\mathbf{S} : \mathbf{S} =_{ij} S_{ij}$ .  $\mathbf{S}$  is defined as:

$$\mathbf{S} = \frac{1}{2}(\nabla \mathbf{u} + \nabla \mathbf{u}^T) \quad (4.9)$$

Even if the net power saving rate is computed from the total dissipation  $\varepsilon$ , the contribution of  $P_f$  and  $P_p$  could be assessed by computing them separately by applying Eq.4.10 and

Eq.4.11

$$P_f = \frac{1}{Re_b S} \int_S \frac{\partial U_t}{\partial n} dS \quad (4.10)$$

Where  $U_t$  is the tangential component of the velocity with respect to the wall surface  $S$ , and  $n$  is the normal direction to the wall.

$$P_p = \frac{1}{S} \int_S p \mathbf{n} \cdot \mathbf{x} dS \quad (4.11)$$

Where  $p$  is the modified pressure  $P/\rho$ ,  $\mathbf{n}$  is the normal unit vector to the wall and  $\mathbf{x}$  is the streamwise unit vector. It's important to highlight that for the plane channel case  $\varepsilon = P_f$ , given that the only mechanism for dissipation is due to friction at the channel walls, and no peristalsis power is required ( $P_i = 0$ ). Returning to the net power saving rate, once the time history of total dissipation  $\varepsilon$  is available, the time averaged dissipation has been computed using expression Eq.4.12. Then the net power saving rate is computed with Eq.4.13 accounting for the time averaged total dissipation for the reference plane channel case and  $\varepsilon_{ref}$  and for the controlled cases with  $\bar{\varepsilon}$ .

$$\bar{\varepsilon} = \frac{1}{t_f - t_i} \int_{t_i}^{t_f} \varepsilon dt \quad (4.12)$$

$$S = \frac{\bar{\varepsilon}_{ref} - \bar{\varepsilon}}{\bar{\varepsilon}_{ref}} \times 100[\%] \quad (4.13)$$

Where  $t_i$  and  $t_f$  are the initial and final external time units respectively. The computed values for the net power saving rates are presented in Fig.4.14, where the horizontal axis is the deformation period in wall units and the vertical axis is the displacement amplitude in both units. The numbers in the left of the parenthesis are the case identification number and the values on the right are the net power saving rates computed, while green circles refer to re-laminarized cases and black triangles to turbulent cases. The case with larger net power saving rate is *case01* with  $S = 64\%$ , followed by the other 2 re-laminarization cases *case02* and *case03* with  $S = 60\%$  and  $S = 56\%$  respectively. *case11*, which is a particular case since the sudden return to turbulence cannot be capture, show a large  $S = 42\%$ , even though it's lower than the complete re-laminarization cases reported by Nakanishi et. al. The ordinary drag reduction cases show lower net power saving rates as expected, reaching *case07*, *case09* and *case10* that don't show any net power saving.

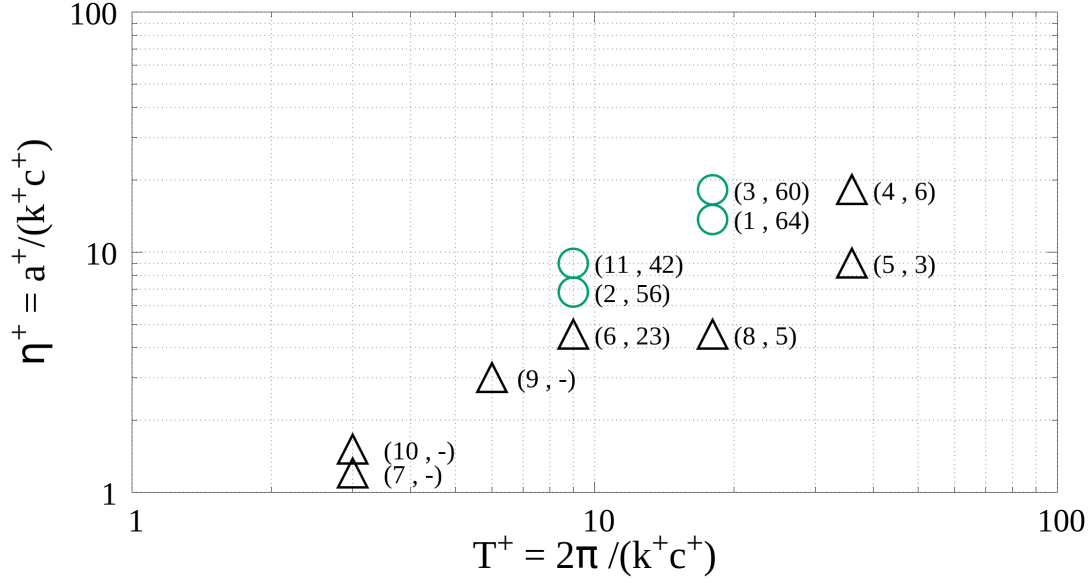


Figure 4.14: Net power saving rate map as function of peristalsis inputs

It's important to observe in Fig.4.14 how the best performing cases are localized in a certain region of the map. This region corresponds to  $T^+ > 8$  and  $T^+ < 20$  with respect to the horizontal axis, and  $\eta^+ > 5$  and  $\eta^+ < 20$ . These results suggest that relaminarization occurs under a relatively large amplitudes of velocity  $a$  and wavenumber  $k$ . However, if the mentioned quantities are further increased, the flow cannot be relaminarized. It can also be observed how very large wave propagation speeds result in no net power savings, as it occurs for *case07* and *case10*. Note that the set of parameters used for the relaminarization cases that perform better in terms of  $S$  coincide with the best performing cases presented by Nakanishi *et. al.*, confirming that the methodology used is suitable for controlling the flow, and as a consequence reducing the net power necessary to drive the flow. Even if the cases for relaminarization, ordinary drag reduction and no net power savings coincide (except for *case05*), there are small quantitative differences between the results in [27] and the ones obtained with the in-house DNS code. Tab.4.4 collects the net power savings computed and its targeted value. Note that  $S$  for the equivalent case to *case11* in [27] is not presented in the reference publication, given that it has the particularity of a cyclic dynamic from laminar to turbulent, and vice versa, that could not be captured by the in-house DNS code. Recalling the comparison of pressure gradients, the results differed because the power required for peristalsis was not accounted for the publication used for validation, while the run-time solution of the simulations performed account for this contribution. Nevertheless, the computation of the net power saving rates was done exploiting the definition of  $S$  based on dissipation for both for the reference and

in the present Thesis. Dissipation at the statistically steady state is defined as the sum of friction power, pressure power and input power. Therefore, the difference in the results in Tab.4.4 doesn't arise from the inclusion of the peristalsis contribution in the mean pressure gradient, but from differences in the numerical approaches implemented.

	S in %	S in [27] in %
Case 1	64	65
Case 2	56	53
Case 3	60	59
Case 4	6	4
Case 5	3	-
Case 6	23	21
Case 7	-	-
Case 8	5	5
Case 9	-	-
Case 10	-	-
Case 11	42	not presented

**Table 4.4:** Comparison between net power savings in % for the in-house DNS code and data reported in [27]

## 5 | Conclusions and future developments

Fully developed turbulent channel flows controlled by means of streamwise traveling waves of wall deformation, also known as peristalsis, have been studied with the aim to validate an in-house DNS code as well as to further understand how the flow behaves in the presence of peristalsis waves and its contribution to net power savings. The in-house DNS solver exploits the Immersed Boundary method over a fixed Cartesian grid for the solid boundaries treatment, leading to a more efficient performance as well as lower memory usage. A three-step Runge-Kutta method with an embedded fractional-step technique has been selected for time advancement of the discretized governing equations. Previously to the validation of the code, the parallelisation scheme has been updated with the MPI library introduction, and a scaling performance analysis has been conducted to use efficiently the HPC resources dedicated to this project.

All the simulations were performed at  $Re_b = 2800$ , and the code was first validated by comparing the computed data with previous studies conducted by Kim, Moin and Moser (1987). Once the reference case was validated, traveling waves of wall deformation were introduced and the majority of the cases included in Nakanishi et. al (2012) were simulated. The solutions obtained are in agreement with the data reported in [27], with the same cases achieving relaminarization except for *Case11*, where the cyclical transition from laminar to turbulent and vice versa could not be captured. In the mentioned publication used as a reference for the peristalsis validation, streamwise traveling waves of wall deformation are proven to be an effective technique for drag reduction leading to net power saving rates, and under certain sets of parameters the flow can re-laminarize. It was also shown that net power saving rates can be achieved for peristalsis configurations where the flow remains turbulent but contributes to ordinary drag reduction. Both observations have been identified in the present project, with *case01*, *case02*, *case03* and *case11* becoming laminar after a relatively short time, while some cases like *case06* and *case04* present net power savings even if they are turbulent for the whole extent of the simulations. The largest net power saving among all cases studied is achieved for *case01*,

with a net power saving of the 64%, while the largest power saving for ordinary drag reduction cases corresponds to *case06*, with 23%. In addition, all the re-laminarization cases have been localized for the input parameters defining the region  $\eta^+ > 5$  and  $\eta^+ < 20$  and  $T^+ > 8$  and  $T^+ < 20$  in the Net power saving rates map.

Even if the best performing cases in [27] are the same cases than for this project, small quantitative differences on the saving results can be observed. A substantial difference in the time traces of mean pressure gradient is also noticed. Nevertheless, the solutions differ because the run-time pressure gradient computed with the in-house DNS code accounts for both the power to drive the fluid flow and the power needed to implement peristalsis. The difference in the net power saving rates is not due to the inclusion/exclusion of this contribution, considering that for both studies it was computed through dissipation rate, which must account also for the peristalsis contribution. Therefore, the differences in the results come from a different numerical implementation for solving the governing equations.

Following the results presented, further research should be performed to identify why the used DNS code is not able to capture the cyclic behaviour from laminar to turbulent, and vice-versa, corresponding to *case12* from [27]. In addition, a more extensive parametric study could bring more information regarding the regions in the new-power saving that result in re-laminarization, and to further understand why the peristalsis inputs show a large decrement in saving rates and how they independently affect the flow. In addition, research of peristalsis techniques have been conducted under a very limited range of Reynolds number, reason why the study of the performance of this particular active flow method with respect to Reynolds number variations could be of great interest to expand even more the capabilities of this prominent method.



# Bibliography

- [1] A. Batikh, L. Baldas, and S. Colin. Application of Active Flow Control on Aircrafts - State of the Art. *International Workshop on Aircraft System Technologies*, Feb. 2017.
- [2] T. R. Bewley. Flow control: new challenges for a new renaissance. *Progress in Aerospace Sciences*, (37):21–58, 2001.
- [3] T. R. Bewley. A fundamental limit on the balance of power in a transpiration-controlled channel flow. *J. Fluid Mech.*, (632):443–446, 2009.
- [4] T. R. Bewley and O. M. Aamo. A ‘win-win’ mechanism for low-drag transients in controlled two-dimensional channel flow and its implications for sustained drag reduction. *J. Fluid Mech.*, (499):183–196, 2004.
- [5] P. W. Carpenter and P. J. Morris. The effect of anisotropic wall compliance on boundary-layer stability and transition. *J. Fluid Mech.*, (218):171–223, 1990.
- [6] H. Choi, P. Moin, and J. Kim. Direct numerical simulation of turbulent flow over riblets. *J. Fluid Mech.*, (255):503–539, 1993.
- [7] P. E. Dimotakis, R. C. Miake-Lye, and D. A. Papantoniou. Structure and dynamics of round turbulent jets. *Physics of Fluids*, (26):3185–92, 1983.
- [8] K. Fukagata, K. Iwamoto, and N. Kasagi. Contribution of reynolds stress distribution to the skin friction in wall-bounded flows. *Physics of Fluids*, (14):L73–L76, 2002.
- [9] K. Fukagata, S. Kern, P. Chatelain, P. Koumoutsakos, and N. Kasagi. Evolutionary optimization of an anisotropic compliant surface for turbulent friction drag reduction. *Journal of Turbulence*, (9), 2008.
- [10] K. Fukagata, K. Sugiyama, and N. Kasagi. On the lower bound of net driving power in controlled duct flows. *Physica*, (238):1082–1086, 2009.
- [11] K. Fukagata, K. Iwamoto, and Y. Hasegawa. Turbulent drag reduction by streamwise

- traveling waves of wall-normal forcing. *Annual Review of Fluid Mechanics*, (56):69–90, 2024.
- [12] R. Garcia-Mayoral and J. Jimenez. Drag reduction by riblets. *Philos. Trans. A Math. Phys. Eng. Sci*, (369):1412–1427, 2011.
- [13] J. M. Hamilton, J. Kim, and F. Waleffe. Regeneration mechanisms of near-wall turbulence structures. *Journal of Fluid Mechanics*, (287):317–348, 1995.
- [14] Y. Hasegawa, M. Quadrio, and B. Frohnappfel. Numerical simulation of turbulent duct flows at constant power input. *J. Fluid Mech.*, (750):191–209, 2014.
- [15] J. Hoepffner and K. Fukagata. Pumping or drag reduction? *Journal of Fluid Mechanics*, (635):171–187, 2009.
- [16] F. Hussain. Coherent structures and turbulence. *J. Fluid Mech.*, 173, 1987.
- [17] M. Kadivar, D. Tormey, and G. McGranaghan. A review on turbulent flow over rough surfaces: Fundamentals and theories,. *International Journal of Thermofluids*, (10):100077, 2021.
- [18] H. T. Kim, S. J. Kline, and W. C. Reynolds. The production of turbulence near a smooth wall in a turbulent boundary layer. *Journat of Fluid Mechanics*, (50):133–160, 1971.
- [19] J. Kim, P. Moin, and R. Moser. Turbulence statistics in fully developed channel flow at low reynolds number. *Journal of Fluid Mechanics*, (177):133–166, 1987.
- [20] S. Kline, W. Reynolds, F. Schraub, and P. Rundstadler. The structure of turbulent boundary layers. *Journal of Fluid Mechanics*, (30):741–773, 1967.
- [21] C. Lee, T. Min, and J. Kim. Stability of a channel flow subject to wall blowing and suction in the form of a traveling wave. *Physics of Fluids*, (20):101513, 2008.
- [22] P. Luchini. Cpl: Compiler and programming language, 2020. URL <https://cplcode.net>.
- [23] H. Luo, H. Dai, P. Ferreira de Sousa, and B. Yin. On the numerical oscillation of the direct-forcing immersed-boundary method for moving boundaries. *Computer and Fluids*, (56):61–76, 2012.
- [24] S. Marella, S. Krishnan, H. Liu, and H. Udaykumar. Sharp interface cartesian grid method i: An easily implemented technique for 3d moving boundary computations. *Jou. of Comp. Physics*, (210):1–31, 2005.

- [25] T. Min, S. M. Kang, J. L. Speyer, and J. Kim. Sustained sub-laminar drag in a fully developed channel flow. *J. Fluid Mech.*, (558):309–318, 2006.
- [26] R. Moarref and M. R. Jovanović. Controlling the onset of turbulence by streamwise traveling waves. part 1: receptivity analysis. *J. Fluid Mech.*, (663):70–99, 2010.
- [27] R. Nakanishi, H. Mamori, and K. Fukagata. Relaminarization of turbulent channel flow using traveling wave-like wall deformation. *International Journal of Heat and Fluid Flow*, (35):152–159, 2012.
- [28] C. S. Peskin. Flow patterns around heart valves: a numerical method. *Jou. of Comp. Physics*, (10):252–271, 1972.
- [29] C. S. Peskin. The immersed boundary method. *Acta Numerica*, 2002.
- [30] S. B. Pope. *Turbulent flows*. Cambridge University Press, 2000.
- [31] M. Quadrio, B. Frohnäpfel, and Y. Hasegawa. Does the choice of the forcing term affect flow statistics in dns of turbulent channel flow? *European Journal of Mechanics B/Fluids*, (56):286–293, 2016.
- [32] O. Reynolds. An experimental investigation of the circumstances which determine whether the motion of water shall be direct or sinuous, and of the law of resistance in parallel channels. *Philosophical Transactions of the Royal Society of London*, (174): 935–982, 1883.
- [33] O. Reynolds. Coherent structures in turbulent flows. *Progress in Aerospace Sciences*, (25):231–269, 1988.
- [34] S. Robinson, S. Kline, and P. Spalart. Review of quasi-coherent structures in a numerically simulated turbulent boundary layer. *NASA Technical Memorandum*, 1989.
- [35] S. K. Robinson. Coherent motions in the turbulent boundary layer. *Annual review of fluid mechanics*, (23):601–639, 1991.
- [36] J. P. Rothstein. Slip on superhydrophobic surfaces. *Annual Review of Fluid Mechanics*, (42):89–109, 2010.
- [37] F. Secchi. Immersed boundary simulation of turbulent flow through a peristaltic actuator. Master’s thesis, Politecnico di Milano, 2018.
- [38] L. Shen, X. Zhang, D. K. P. Yue, and M. S. Triantafyllou. Turbulent flow over a flexible wall undergoing a streamwise traveling wave motion. *J. Fluid Mech.*, (484): 197–221, 2003.

- [39] Y. T. R. Mittal, H. S. Udaykumar, and W. Shyy. An accurate cartesian grid method for viscous incompressible flows with complex immersed boundaries. *Jou. of Comp. Physics*, (156):209–240, 1999.
- [40] S. Taneda and Y. Tomonari. An experiment on the flow around a waving plate. *Journal of the Physical Society of Japan*, (36):1683–1689, 1973.
- [41] P. Viswanath. Aircraft viscous drag reduction using riblets. *Progress in Aerospace Sciences*, (38):571–600, 2002.
- [42] M. Walsh. *Turbulent boundary layer drag reduction using riblets*. 1982.

## Acknowledgements

First and foremost I am extremely grateful to my supervisor Maurizio Quadrio, for giving me the opportunity to develop this work under his guidance and for all the valuable knowledge and experience provided throughout the Thesis. I would like to also thank Francesco Secchi, for helping me to continue his work.

I cannot thank my whole family enough, and especially to my parents, my sister and my aunt for the constant support they have shown during all my academic career. You've always been by my side no matter the situation, encouraging me to pursue my objectives. Thank you for all the values that you have taught me during my life, and that have shaped the person that I'm today. In this moment I cannot but think about *la Iaia*, I know you would be the proudest person in the world.

Rita, I am deeply grateful for your love and support. Thank you for being a part of my life, for inspiring me every single day, and for making the distance between Barcelona and Milano disappear when I needed it the most. This work wouldn't have been possible without you by my side, and I look forward to keep accomplishing our goals together.

A heartfelt thank you to my dear friend Adi for all the hours we've spent together, either studying or hanging out. You can understand better than anyone how tough this journey has been, and I'm truly grateful to have shared this long path with you. Clara, *mil gràcies*. You were completely right, we could have never imagined back in Terrassa all the experiences and good times that were awaiting for us in Milano. Thank you for making me feel at home. To Cristina, Juan, Nico, Fiodo, Giacomo, René, Claudia, Madda, Matte, Andy, Icar, Ale, Fede and every single person I've met during these years in Milano. I feel very fortunate to have met so many inspiring and caring people who I can call friends.